The Pennsylvania State University
The Graduate School
Department of Electrical Engineering

ENERGY MONITORING AND CONTROL OF HARMONIC GENERATORS FOR LIDAR APPLICATION

A Thesis in
Electrical Engineering

by
Stephen O. Sprague

Submitted in Partial Fulfillment
of the Requirments
for the Degree of

Master of Science

May 1995

We approve the thesis of Stephen O. Sprague.

Date of Signature

_____ _____

Charles R. Philbrick
Professor of Electrical Engineering
Thesis Advisor

_____ _____

Timothy J Kane
Assistant Professor of Electrical Engineering

_____ _____

Larry C. Burton
Professor of Electrical Engineering
Head of the Department of
Electrical Engineering

Abstract

This thesis presents the design and development of a laser energy monitor which accomplishes the task of continuously measuring the laser's pulse energy and providing information for the tuning of harmonic generating crystals. The new energy monitor demonstrates its usefulness in a lidar system developed at Penn State for continuous use onboard Navy ships. However, the goal was also to design a simple and cost-effective device that could be useful in several other applications.

The energy monitor accomplishes simultaneous measurements of a laser's power at two harmonic frequencies. Volume scattering in a glass window as the beam passes through provides a simple means of obtaining a constant fraction of the laser's energy per pulse. A peak detector circuit changes the pulsed signal to a DC signal that is linearly proportional to the laser's power. This measurement both characterizes the laser's performance and allows an automatic control sequence to "peak" the harmonic generators. The designed control system will optimize these harmonic generators one at a time with a modified gradient, adaptive step size algorithm. Simulation software offers a good environment for modeling the oddities of a particular harmonic generator and for testing the control algorithm.

The energy monitor and control designs were driven by requirements of the LAPS (Lidar Atmospheric Profile Sounder) system. Final results verify the proper operation of the energy monitor and suggest its usefulness in other applications. Also, the tuning of the harmonic generators in the LAPS system can be taken as an approach to optimizing other systems that depend upon nonlinear crystals for harmonic generation.

Table of Contents

List of Figures

List of Tables

Acknowledgments

I recieved invaluable support for my thesis and other help in achieving my Master's degree. The support came in the form of classroom instruction, but also in the casual conversations that carried me through each day. Much of what I learned came from these conversations and the time others took to simply talk with me. In particular I would like to acknowledge those other members of "Team Lidar": B. Smith, S. Rajan, G. Pancoast, T. Petach, T. Stevens, P. Haris, M. O'Brian, G. Evanisko, R. Harris, and S. Mathur. I could not have finished my thesis without your help.

My thesis advisor, C. R. Philbrick, provided a place for me to work, a project to work on, and guidence in all my studies. He challenged me to do more than I would have done on my own, and I am grateful for his help. I am also indebted to Dr. Timothy Kane for answering my endless questions from the first time I arrived at Penn State.

I thank my wife, Andrea, for suffering through much of this thesis with me. And, finally, I would like to acknowlegde my Lord and Savior Jesus Christ apart from whom I do nothing right.

Chapter 1

INTRODUCTION

As high power lasers find increasingly more applications in industry, so must engineers find simple, cost-effective ways to monitor and optimize the laser's operation. Commonly used power meters intercept the entire beam for infrequent spot checks of the output energy. These can be damaged as they take the full intensity of the laser's beam. There are several simple approaches to detecting a constant fraction of the lasers energy and recording it; yet, a practical, flexible, and inexpensive method has not establish itself in the marketplace. With this goal in mind, a new energy monitor has been demonstrated in a lidar system developed at Penn State University for the U.S. Navy.

The shipboard LAPS (Lidar Atmospheric Profile Sounder) system will measure atmospheric properties on a regular basis. This differs from the lidar's common use as a research instrument. The constant use of the system calls for a rugged design with many automated features. An automated subsystem for monitoring and optimizing the laser source is vital to the entire system's operation.

An integrated energy monitor involves the development of both an opto-mechanical and electo-optical design. The monitor supplies a computer with analog DC signals proportional to the laser's power at two or more harmonic frequencies. In addition to providing a measure of system performance, this monitor serves as a feedback sensor in a control loop that "peaks" the harmonic generators. To achieve this optimization, a measure of the power output at the harmonic frequency must be made after the pulse has passed the harmonic generating crystal. A control algorithm will then optimize the performance by peaking the energy output at the harmonic frequencies. Simulation software offers a good environment for modeling the oddities of a particular harmonic generator and for determining an intelligent control algorithm.

This thesis deals with the monitoring and control of the laser in the LAPS system; however, it could also improve the operation of several research lidar systems or any application that uses a high power laser. The basic design provides a simple, flexible, and

inexpensive device. Application to the LAPS lidar system serves as only one example of the potential usefulness of the subsystem developed in this thesis.

1.1. Lidar Principles

A variety of instruments have been developed over the years to record information on Earth's atmosphere, but lidar (LIght Detection And Ranging) offers the greatest promise as a remote sensing instrument to study atmospheric dynamics, structure parameters, and species. Some of the world recognized atmospheric concerns are the degradation of the ozone layer and the steady increase of CO_2 concentrations. In addition to the lidar's contribution to basic measurements in these areas of research, a laser remote sensing instrument has the inherent ability to offer very high temporal and spatial resolution in the measurements of properties like temperature and water vapor, which can not be obtained from the more conventional radiosonde balloon measurements.

As a brief description of the lidar technique, let us consider high intensity laser pulse with its electric field, **E**, propagating in the z direction and polarized at an angle ϕ from the y axis. As the energy E propagates through a sample of thickness Δz, a fraction of the incident energy, ΔE, scatters along the direction at an angle theta from the z axis. Figure 1.1 shows the coordinate system and schematic of the scattering process. A value for this scattered energy depends on the scattering process and the geometry in question, but a general expression is,

$$\Delta E = n E \left[d\sigma(\theta,\phi)/d\Omega \right] \Delta\Omega \Delta z, \qquad (1\text{-}1)$$

where n is the molecular density, $d\sigma(\theta,\phi)/d\Omega$ is the differential cross-section of the scattering process, and $\Delta\Omega$ is the detection solid angle [Measures, 1984]. Since most lidars place the receiver telescope in the same spot as the laser source, the backscattering cross-section, $d\sigma(180°,\phi)/d\Omega$, is of interest. Due to the symmetry, this cross-section and corresponding backscattered energy are independent of the polarization, ϕ. The discussion in Chapter 2 on scattering in glass as a bulk medium will return to this concept.

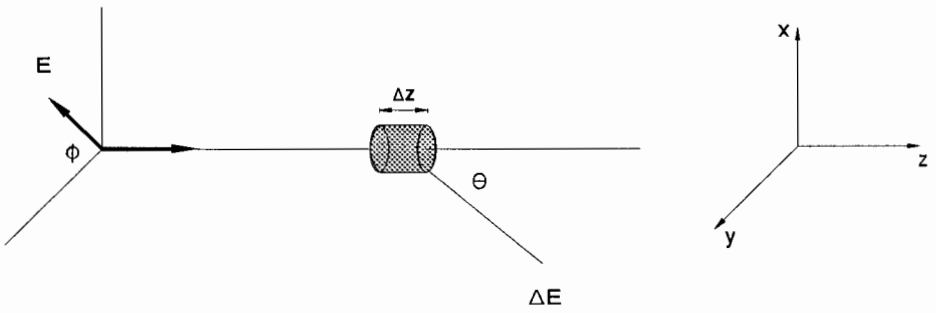

Figure 1.1. Differential scattering cross-section for an electric field, E, propagating in the *z* direction and polarized at an angle ϕ from the *y* axis.

In that case, however, the scattering cross section will be $d\sigma(90°,\phi)/d\Omega$, and the scattered energy will be *dependent* on the polarization.

Again, the differential cross-section will depend on the process that describes the scattering of the laser radiation as it interacts with matter. The scattering may include particles ranging in size from much smaller than the laser wavelength ($a \ll \lambda$) to much greater than the laser wavelength ($a \gg \lambda$), and they could have a spherical, irregular, or crystalline shape. These characteristics and their combinations define a variety of scattering processes. One scattering process which is of primary importance later in this thesis is molecular Rayleigh scattering ($a \ll \lambda$) of the central Cabannes line. Scattering of the Cabannes line can be described as "elastic," since the internal molecular energy remains unchanged in the process [Young, 1982].

Raman scattering describes another type of scattering where the energy does change, resulting in a scattered wavelength that is shifted from the Cabannes line. Here, the wavelength shifts are proportional to changes in vibrational and rotational energy states of the molecular specie in question ($\nu = \Delta E/\hbar$). If you start with molecules at an arbitrary ground vibrational ground state, incident laser light elevates the molecules to an

excited virtual state. A small fraction of these events may then spontaneously decay to another vibrational state of higher or lower energy than the ground state. That decay, ΔE, is characteristic of the Stokes and anti-Stokes lines for a particular molecule, depending on whether the new energy level is less than or greater than the ground state, respectively. Each Stokes and anti-Stokes line has a distribution of narrower lines around it that correspond to changes in the rotational energy states or rotational Raman scattering [Measures, 1984]. The LAPS system utilizes both vibrational and rotational scattering to obtain atmospheric data.

1.2. Penn State's LAPS System

Lidar has demonstrated its ability to make temperature and water vapor measurements that could simply replace the use of weather balloons for those profiles. Such lidar measurements are especially applicable to the platforms where frequent measurements are needed, like Navy vessels. Refractivity in the atmosphere is derived from molecular density (from the temperature measurements and surface pressure measurements) and water vapor concentrations. The detection of refractive layers can then predict the ducting of radar signals. An afloat lidar system can contribute continuous measurements to a data base of weather information and minimize the use of disposable weather balloons.

Although lidar systems around the world have measured temperature and water vapor successfully, a shipboard system requires the added and special features of compactness and automation. Topside space on a Naval vessel is at a premium, so minimizing the size and amount of LAPS equipment on the deck of the ship was an essential criterion. Figure 1.2 is a picture of the deck unit with it's major components, the larger of which are the laser and receiving telescope. The energy monitor and crystal tuning discussed in this thesis reside locally on this deck unit, the first as an instrument placed at the output end of the laser and the second as a software function stored in the deck unit computer. Automated subsystems will control the laser source, data processing, safety features, and climate. During normal operation, an operator will

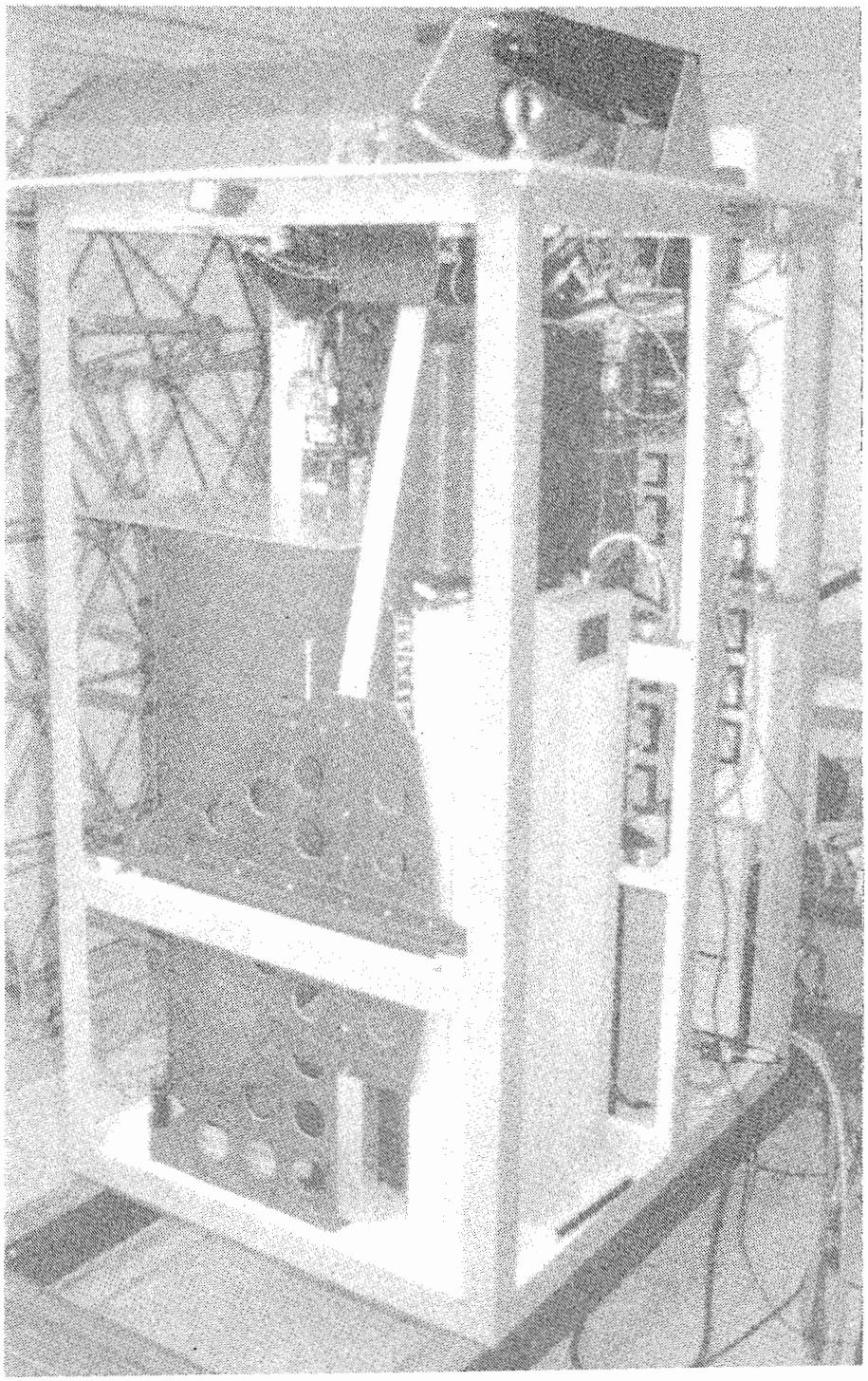

Figure 1.2. Picture of the LAPS deck unit with side panels removed. Telescope mirror is at the base of the cylindrical structure, and the laser is mounted on the opposite side of the optical table. An electronics rack to the right of the laser houses the deck unit computer and other laser electronics.

monitor and make adjustments to the system at a console which lies below the deck of the ship. Fiber optic communications, power, and cooling water connect the deck unit to the equipment in the console's room. Therefore, apart from periodic repair and maintenance, only these links provide access to the deck unit. This LAPS requirement stresses the need for remote energy monitoring and automated laser control.

The primary function of this first phase of LAPS is to make temperature and water vapor measurements based on rotational and vibrational Raman scattering, respectively. The temperature measurements follow from determining the relative population distribution of the pure rotational Raman energy states, because the distribution directly depends on the temperature exciting the molecules. At the 532 nm laser output, the first Stokes vibrational Raman scattered wavelength for H_2O molecules is 660 nm and that for N_2 is 607 nm. Water vapor concentrations are derived from the ratio of these two signals. An important dilemma is that the water vapor measurements which come from the 532 nm laser output are limited to the nighttime. Otherwise, the sunlight background provides too much signal in the visible part of the spectrum. To overcome this background, the quadrupled output of the Nd:YAG laser (266 nm), which radiates in the solar blind region of the spectrum, provides a strong enough signal to noise ratio for daytime measurements. Therefore, the laser source must, as a fundamental requirement of the system, generate the 2nd and 4th harmonics of the laser's output using nonlinear crystals.

The source in this system is a flashlamp-pumped, Q-switched Nd:YAG laser, Continuum model 9030. The laser operates at 30 Hz with an average power of 48 Watts at the fundamental wavelength of 1064 nm. At that wavelength the output is 1.6 Joules per pulse with a pulse width of about 7 nanoseconds. The laser's power electronics are located next to the laser in the deck unit, and a deck unit computer controls the operations of the laser via an RS232 port. Among those operations are the timing, firing, safety switches, and crystal tuning. Harmonic generating crystals double and quadruple the frequency of the fundamental for a combined output. The frequency doubling crystals are described in Chapter 3, but for now we accept that the output beam includes about 13 watts at 532 nm and 3.5 watts at 266 nm when the crystals are properly tuned.

Beamsteering mirrors direct the beam over the mirror and vertically through a coated glass window.

The laser will need to operate for data collection runs on a regular interval. The backscattered signal is dependent on the source power, and thus the lidar system needs to maintain a constant source of power at the harmonic frequencies (532 nm and 266 nm) during a data run. From time to time the crystals will fall off their maximum conversion efficiency. If this happens, an operator normally makes a spot check of the laser's power with a power meter and then adjusts or tunes the crystal before the next data run. The LAPS system, however, requires the topside unit to operate without the assistance of a laser operator. Among other automated features, LAPS calls for an energy monitoring and tuning system that can act independent of a laser operator.

1.3. Outline of Thesis

This thesis will describe the background, design, and implementation of an energy monitor and crystal tuning system. Chapter 2 discusses the energy monitor. It begins with the design criteria and process, describes the opto-electronics of the instrument, and demonstrates the its usefulness and limitations. Chapter 3 concerns the design of a control system to automatically tune the nonlinear crystals. This chapter first provides an introduction to nonlinear crystals and harmonic generation, followed by a characterization of the actual laser system. Finally, a control algorithm is developed and tested in a software simulation. Chapter 4 presents the broader application of the energy monitor and tuning control system to other laser systems.

Chapter 2

ENERGY MONITOR

With a vast array of inexpensive detectors on the market, monitoring the energy of a high power laser would seem a straightforward and simple task. However, it is the requirement to continuously monitor a high power output which makes the task more difficult. Frequently, the laser energy is measured using a power meter which depends upon a calorimeter technique. These devices offer only intermittent checks of the beam, because they intercept the complete beam. Even power meters rated for high power can still burn or break under the intense energy. Furthermore, use of power meters would require beamsplitters to examine the power at each of the wavelengths. LAPS, however, calls for the monitoring of two wavelengths continuously and without interrupting the beam.

The monitor must measure the energy changes reliably. For a device that has a linear response to a range of optical intensities, both the optics and electronics must be linear. This chapter will show that the volume scattering solution and the peak detector circuit can provide a simple, reliable, and inexpensive design. Finally, calibration against a power meter will demonstrate the linearity of the device which has been designed.

2.1. Fundamental Design Alternatives

The basic requirement of the design is to sample a small fraction of the laser's energy and separate the sampled energy into two channels for measurements at the 532 nm and the 266 nm wavelengths. The signals must be of an optical intensity that lies within the linear range of the detector.

Figure 2.1 shows three design alternatives, each of which could fit inside the laser housing and just after the harmonic generating crystals. All three designs include a glass window in the path of the beam. These windows need to be of a special quality of optics, called laser optics, due to the intensity of light approaching optical damage thresholds of the materials and coatings. In each case, UV-grade synthetic fused silica makes a window

that is relatively inexpensive, relatively free of imperfections, and able to transmit efficiently at ultraviolet wavelengths. From Chapter 1, the laser outputs a pulse with 800 mJ of green light (532 nm) and 130 mJ of ultraviolet radiation (266 nm). For a 6 ns pulse and a 9.5 mm beam diameter, the surface intensity is about 150 MW/cm^2 and 75 MW/cm^2, respectively. (A beamsplitter placed after the second harmonic generator reflects most of the power at the fundamental infrared wavelength into a water-cooled beam dump). An additional consideration for use of this laser optic is the polarization of the incident light. The nonlinear effect of the second harmonic generating crystal rotates the circularly polarized beam at 1064 nm to vertically polarized green light. The fourth harmonic generating crystal then rotates the polarization of the green light to horizontally polarized UV radiation. Both harmonics with their respective polarization are present at the energy monitor's window.

Figures 2.1(a) and 2.1(b) show a thin window placed at an angle of incidence of 45°. The supplier of this optic would use an anti-reflecting coating on both surfaces of the optic to minimize losses to the output laser beam. As most of the beam's energy passes through the window, only about 0.5 to 1.5% of the radiation at both wavelengths will reflect off each surface of the window. As a sidenote, when the light is parallel to the plane of incidence, the Fresnel reflection coefficient can be further minimized for an uncoated window at 56.3° (Brewster's angle) to the direction of propagation. However, any savings on an uncoated window would be offset by a waveplate to rotate the green light to a horizontal polarization. Regardless of whether the window is coated or not, the sampled energy will have some dependence upon the reflection at both surfaces of the widow. Changes at a window surface (i.e. surface dust, aging of the coating, smudges, ...) could alter the energy reflected and limit the long term stability of the detector.

Figure 2.1(a) shows the 45° window which will reflect a sample of the laser's beam for filtering and detection. The power must be sampled at two wavelengths, thus the second optical element in this design is a diffuser. The diffuser is an inexpensive ground glass that spreads the collimated beam in three dimensions. Both the 532 nm and 266 nm channels are geometrically arranged to receive a portion of that diffused light. Each

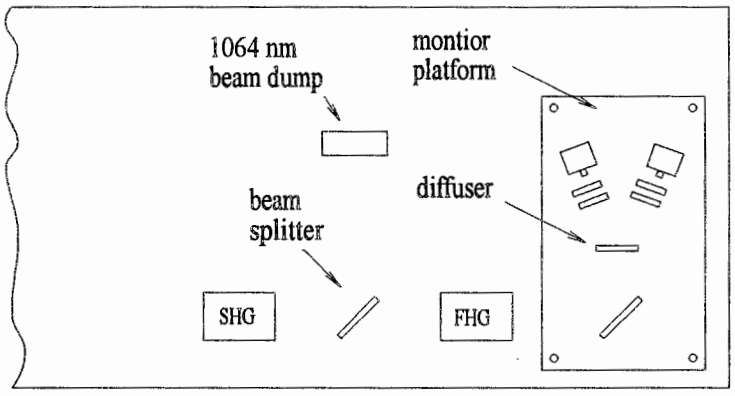

(a)

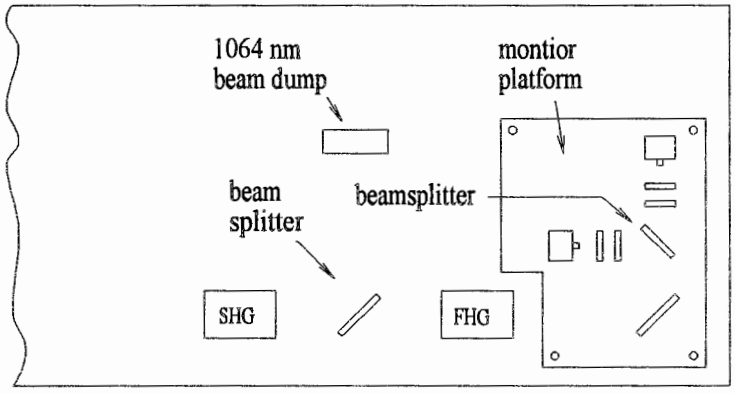

(b)

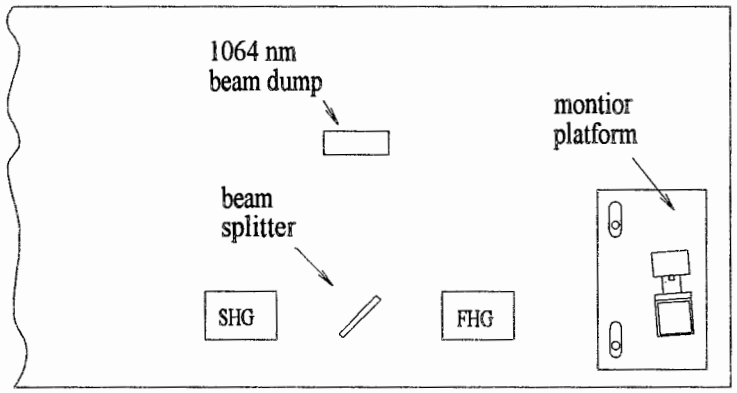

(c)

Figure 2.1. Energy monitor design alternitives: (a) using diffuser, (b) using beamsplitter, and (c) volume scattering method.

channel includes a bandpass filter specific to the channel wavelength. Each channel also uses a neutral density filter(s) in which the transmitted radiant power (T) relates to the optical density (D) as $T = 10^{-D}$. The neutral density filters bring the light intensity into the linear range of the detector. Replacing or adding to the neutral density filter make the final adjustments to this design very easy. However, Figure 2.1(a) does not show light-tight channels which may be required to reduce the detection of stray reflections inside the laser housing [Evanisko, 1994].

The second design in Figure 2.1(b) differs from the previous design only in the way that it separates the two channels. An ideal beamsplitter could, for example, reflect all the power at 532 nm and transmit all the power at 266 nm. This optic would eliminate the need for separate bandpass filters. However, the cost of such a dichroic beamsplitter would outweigh the money saved from not buying bandpass filters. Any sort of beamsplitter (40/60, 50/50, power beamsplitter, ...) could be used provided that the filters are used. This design maintains the collimation and diameter of the original beam, unlike the previous design. The beam diameter is 9.5 mm, which is larger than the active area of most silicon detectors. Therefore, an additional optic (not pictured) must either focus the beam to collect all of the energy on a smaller detector or diffuse the beam to eliminate "hot spots" in the beam. Again, this design will need neutral density filters to bring the light into the linear range of the detector and a light-tight assembly to block any stray energy.

An inherent disadvantage of the first two designs is associated with the coated window in the laser path. The AR coatings both maximize the power transmitted and minimize the power reflected. That may sound redundant, but both are important functions. Maximizing the output of the source is obvious, but why reduce the reflectance to 1% or less when that is the fraction of light for detection? Simply, it is too much power. The fraction of light is 1% of about 250 MW/cm^2 or 2.5 MW/cm^2. That is still sufficient power to require laser quality optics in the next stage of components (in this case, diffuser or beamsplitter), because standard inexpensive optics may fail. Furthermore, a typical silicon detector has a linear response in the range of mW or μW. Significant,

perhaps expensive, filtering must stably attenuate the power to an acceptable order of magnitude.

The final design in Figure 2.1(c) operates under the principle of volume scattering in a glass window. The power that scatters out the edge of a thick (½") window is orders of magnitude less than the 1% reflection from a coated glass surface. For a rough estimate of the scattered power, many fiber optic companies have transmittance curves where the beam extinction at wavelengths less than 600 nm is predominately due to scattering losses. At the edge of the scattering window is a filter assembly and detector box for each channel. The filter assembly mounts to the scattering block and holds ½" diameter bandpass and neutral density filters. The detector box then mounts to filter assembly for a light-tight and compact design. There is no need for the second-stage diffuser or beamsplitter, and the scattered intensity is at a manageable intensity for non-laser optics. Furthermore, the amount of light detected depends upon the volumetric scattering within the window material, and the does not depend directly upon window surfaces as in the first two designs. This design should result in a more stable, self-contained, and compact unit.

2.2. Scattering Basics

Intrinsic to the third and final design is an understanding of the scattering process within the glass window. Initial calculations of the energy scattered, based on the transmittance curves in fiber optics of similar glass, show that the ½" optic will scatter sufficient energy for detection. But, what kind of scattering is it? What is the scattering pattern? Is the process linear, and does it depend on the polarization of the incident beam? The following mathematical explanation and laboratory results answer these questions and support the design.

From Equation (1-1), the differential scattering cross-section is a function of the scattering process and geometry. For a filter assembly and detector facing the edge of the scattering block, the 90° cross-section, $d\sigma(90°,\phi)/d\Omega$, is now of interest. Unlike the backscatter cross-section, the energy detected now depends on ϕ, the polarization of the

incident electric field. For a given polarization there is a characteristic scattering pattern.

A monochromatic electric field induces a dipole moment in a molecular specie when the electrons are forced into oscillation at the frequency of the electric field. That dipole moment then acts as its own source and distributes the energy of the incident field as it radiates electromagnetic energy in a characteristic pattern. The Poynting vector, as shown below, is the rate at which electromagnetic energy crosses a unit area whose normal is parallel to $\boldsymbol{S}$,

$$\boldsymbol{S} = \epsilon_0 c^2 \boldsymbol{E} \times \boldsymbol{B}. \tag{2-1}$$

Using spherical coordinates, the resulting Poynting vector can be represented as,

$$\boldsymbol{S} = \hat{\boldsymbol{R}} \left(\frac{\sin^2\theta}{16\pi^2 \epsilon_0 c^3 R^2} \right) \left[\frac{d^2}{dt^2} p\left(t - \frac{R}{c} \right) \right]^2 \tag{2-2}$$

where p is the electric dipole moment, and θ is the angle between the dipole axis and the vector $\boldsymbol{R}$. An important result from this formula is the radiation pattern, $\sin^2\theta$, particular to a linear electric dipole oscillator. Figure 2.2 shows three-dimensional picture of this pattern for two different polarizations. Theoretically, there is no radiation parallel to the axis of the dipole, and the maximum radiation occurs normal to the dipole axis.

The laser system for LAPS delivers vertically polarized 532 nm light and horizontally polarized 266 nm radiation, with their respective ideal dipole radiation patterns are depicted in Figure 2.2. Therefore, energy monitor design orients the filter assemblies and detectors so that the 532 nm channel looks at the window's edge from the side and the 266 nm channel looks down from the top. Although it is not part of the design, a 1064 nm channel could be placed at any edge of the window, because the 1064 nm beam is circularly polarized.

The total power radiated is obtained by integrating across a spherical surface the rate of energy through that surface,

$$Pwr = R^2 \int_0^{2\pi} d\phi \int_0^{\pi} d\theta \sin\theta \, \boldsymbol{S}(R,\theta,\phi) \cdot \hat{\boldsymbol{R}} \tag{2-3}$$

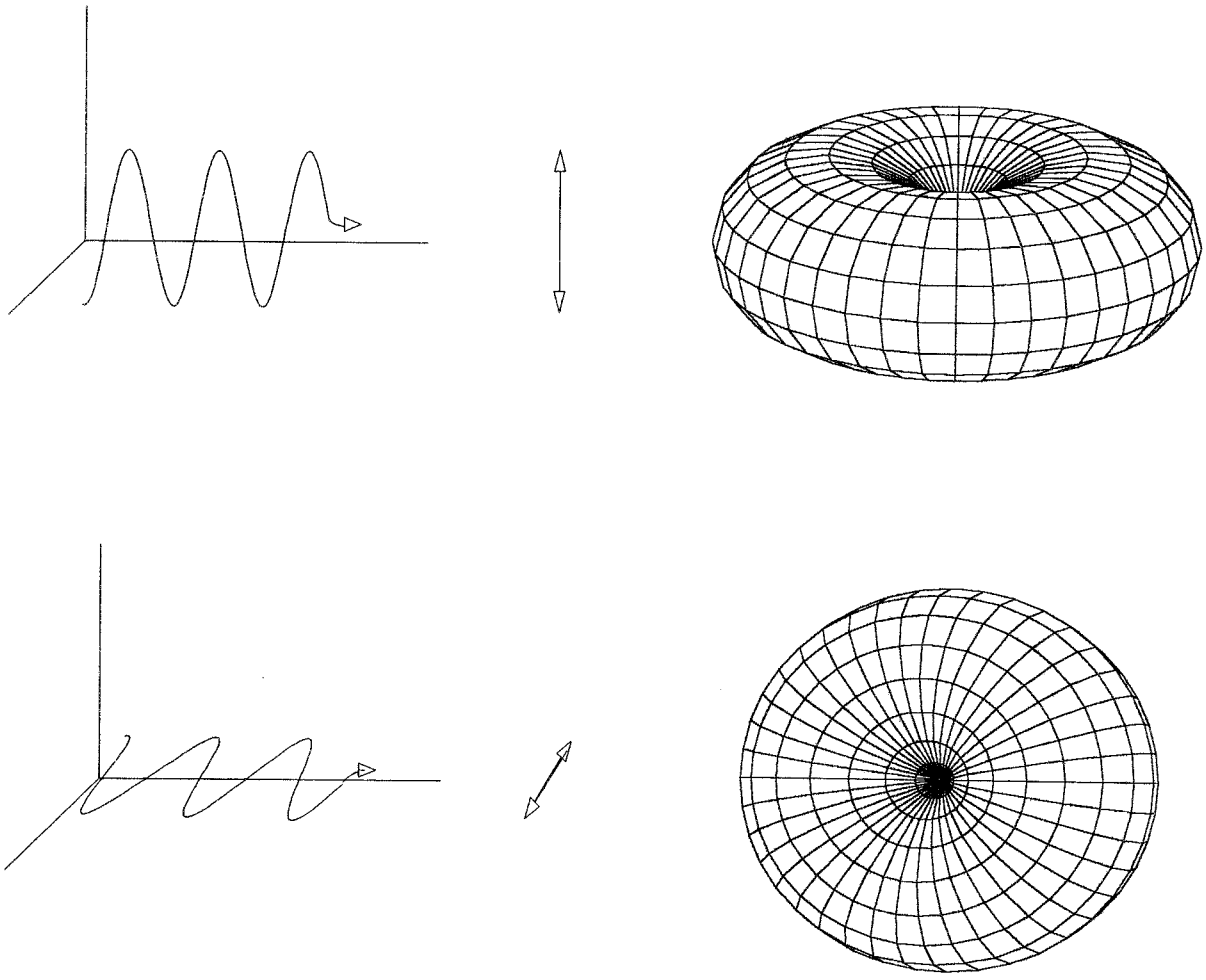

Figure 2.2. The characteristic dipole radiation pattern is on the right for both a vertically polarized and a horizontally polarized electric wave.

For $\boldsymbol{S}$ found in (2-2), the total power radiated by the dipole is

$$Pwr = \left(\frac{1}{4\pi\epsilon_0}\right)\frac{2}{3c^3}\left(\frac{d^2p}{dt^2}\right)^2. \tag{2-4}$$

The following representation of the dipole moment assumes a monochromatic plane wave traveling in the z direction and an atomic dipole polarizability, $\alpha(\omega)$,

$$\boldsymbol{p} = \frac{\boldsymbol{P}}{\boldsymbol{N}} = \hat{\boldsymbol{x}}\alpha(\omega)E_0\cos\omega(t-z/c). \tag{2-5}$$

Therefore, the instantaneous power radiated by a single dipole becomes,

$$Pwr = \frac{8\pi^3 c}{3\epsilon_0\lambda^4}\alpha^2(\omega)E_0^2\cos^2\omega(t-z/c). \tag{2-6}$$

This power can be rewritten in terms of the Poynting vector of the incident field as,

$$Pwr = \frac{8\pi^3}{3\epsilon_0^2\lambda^4}\alpha^2(\omega)\,|\boldsymbol{S}|. \tag{2-7}$$

Equation (2-7) shows that the power radiated from the electric dipole is linearly proportional to S, the power per unit area of the incident field. They are related by a constant of proportionality which has the units of area. This area is called the scattering cross-section and is given by,

$$\sigma = \frac{8\pi^3}{3\epsilon_0^2}\alpha^2(\omega)\frac{1}{\lambda^4}. \tag{2-8}$$

Up to this point, the development has dealt with a single scatterer. However, the glass

window in the energy monitor serves as a continuous medium with a number of scatterers. Equation (2-8) can then be written in terms of the index of refraction, $n(\omega)$, and the density, N, of the medium,

$$\sigma = \frac{8\pi^3}{3}\left(\frac{n^2(\omega) - 1}{N}\right)^2 \frac{1}{\lambda^4}. \qquad (2\text{-}9)$$

Most notable in this equation is how the scattering cross-section changes with wavelength. For example, it shows that radiation at 266 nm will scatter 16 times as much as light at 532 nm. The λ^{-4} dependence of this scattering cross section is commonly associated with the term Rayleigh scattering; however this is somewhat of a misnomer. Equation (2-9) applies to the elastic scattering of the central Cabannes line, but the work by Lord Rayleigh applied not only to the elastic, λ^{-4} scattering but also to the Stokes and anti-Stokes lines from rotational energy changes in the specie [Young, 1982].

Up to this point, the development has assumed the dipole radiation pattern of a molecular scattering. However, other types of scattering are present. The inelastic scattering in a glass window is minimal, and the filters look only at the unshifted lines. Molecular and particulate scattering can occur at the unshifted lines, but the latter would not exhibit the radiation pattern from Equation (2-2). After the energy monitor was constructed, the filter assemblies were switched to test the radiation pattern, and the lab test resulted in a quarter the amount of scattering in this orientation. Therefore, the scattering pattern approximated that of dipole scatterers. In addition, the transmittance curves for this glass material show a λ^{-4} dependence for wavelengths below 600 nm. Therefore, the molecular scattering is the dominate scattering mechanism which supports the assumption made earlier.

2.3. Peak Detecting

The Continuum Powerlight 9030, like many Nd:YAG lasers, makes use of Q-switching to generate high intensity pulses with extremely high peak power compared to

what a continuous mode laser could achieve. The laser outputs 6 ns pulses 30 times a second. The energy monitor detects these pulses from the scattered energy as the pulse passes through the window. The electronics, then, must supply the computer database with a measure of the laser's power. The calorimetry method effectively measures the time average of many pulses, but more options are available with high speed electro-optics.

The electro-optic design began with the selection of a detector. Silicon photodiodes are available inexpensively and in various arrangements. They can either be PIN photodiodes or avalanche photodiodes, the later of which is more sensitive than the energy monitor requires and has more noise associated with it. In the PIN construction, the P and N type silicon materials are doped with excess free charge carriers, and a lightly doped intrinsic bulk silicon of either P or N type forms the depletion region in-between the P and N materials. When the semiconductor is illuminated in the depletion region, hole-electron pairs are created and swept to opposite sides of the depletion region creating a current that is proportional to the intensity of light. The HUV-1100BQ from EG&G is a typical silicon PIN photodiode with the added features of UV enhancement and built in amplification (see Appendix A for a technical sheet on this part).

The design of the HUV-1100BQ is for low frequency to DC detection, so it will not be able to detect the pulse shape of a 6 ns pulse. This is not a problem, however, because the photodiode has the effect of simply spreading out the pulse in time. The 6 ns pulse resulted in a pulse on the output stage of the detector with a 50 μs rise time and a 200 μs fall off (the shape of this spread pulse did not change with the intensity of light). Electronics may then record the peak of that pulse or integrate under the pulse. In either case, the response is linear to the intensity of light that illuminates the detector surface. The slow time response of the detector does not adversely affect measurements of the 6 ns pulse. This is not true of the photocell which may not detect the presence of a fast pulse.

The next stage of the design is the electronics which, as noted above, either detect the peak of the pulse or integrate under the pulse. A simple integrator circuit could use a capacitor to integrate, a sample/hold chip to hold the integrated value, and a MOSFET switch to turn on the sample/hold chip during each pulse. However, the energy in each

pulse is more information than is required. The energy monitor built relies on the peak detecting method. One obvious way to record the peak is simply for the computer to sample the pulse when it reaches a peak voltage. However, this would mean synchronizing the energy monitor with the timing system of that particular laser or lidar system. For the energy monitor to be applicable to other systems, a detector circuit could supply the A/D board on the computer with a DC value proportional to the laser's power. The need, in this case, is for a peak-detector circuit that holds the peak pulse from the output stage of the actual detector.

Among the general design requirements of this peak-detector circuit were output range, noise isolation, and time response. In the LAPS system, the computer A/D board encodes inputs which must lie between 0 and 10 volts (V). For the best resolution, the circuit's full scale output would be close to the maximum 10 volts. The circuit, itself, does not adjust the output range, but neutral density filters attenuate the optical signal reaching the detector. Again, the ultimate objective of the energy monitor is to provide a voltage *linearly* proportional to the optical power.

The noise isolation of the circuit is especially important given the high power electronics running the laser. Large currents pulse an electro-optic modulator to achieve Q-switching, and the high dI/dt results in large electro-magnetic noise generation. To reduce the effect of the noise, the design calls for a metal chassis, twisted shielded pair for the signals, and a separate ground wire for the power supply. Each circuit board will then have three input lines (+12V, -12V, and GND) and two output wires (SIGNAL and GND).

The time response of the circuit depends on the speed with which the circuit can follow changes in optical intensity. This is fundamentally limited by the pulse repetition rate of the Q-switch in the laser, 30 Hz. Therefore, every 33 ms the energy monitor will detect a new pulse. An ideal peak-detector circuit will follow the upward slope of the pulse (infinitely fast slew rate) and hold the peak value indefinitely. If each succeeding pulse were higher than the previous pulse, then the time response of the circuit would be no slower than the 33 ms between pulses. However, the circuit must follow drops in

optical power, too. The rate at which the non-ideal circuit falls off the peak is sometimes called droop, and this becomes the limiting factor in the time response of the circuit. Figure 2.3 gives a picture of the optical pulses, the spread pulses at the detector output, and the output of a peak detector circuit with some droop.

The design objectives for this circuit's time response are, then, for a slew rate faster than 200 V/ms and a droop rate approximately equal to 2 V/s. A slew rate of 200 V/ms is fast enough to follow full scale pulses (10V) to the peak in 50 μs. Therefore, the natural spreading of the laser pulse by the detector is actually of benefit to the design of the following circuit. If the computer samples the circuit's output at some unknown time after each pulse, then the droop must be negligible in-between two pulses. For a drop in optical power, the detector may show a pulse to pulse drop from 7 volts to 5 volts. Between these two pulses the circuit would fall off (2 V/s)×(0.033 s) = 0.066 V or less than 1% off the peak. In one second, however, the circuit will follow the drop down to the 5 volt level. If we assume that the 2 volt drop between pulses (as seen by the detector) is the maximum rate at which the optical power will fall, then the time response for a circuit designed for a 2 volts/sec droop rate is one second.

The simplest form of a peak detector circuit consists of a diode and capacitor as shown in Figure 2.4(a). The capacitor charges on the upward slope of the input until the peak. After the peak, the diode will become reversed biased, and the capacitor will hold the charge. However, this circuit has some significant drawbacks. First, the diode limits the circuit from detecting peaks less than 0.6 volts, the forward voltage drop of a typical diode. This narrows the output range of the circuit to one decade and, thus, diminishes resolution. Secondly, the input impedance is very low when the input approaches a peak voltage. In general, the circuit should have a high input impedance and a low output impedance.

Figure 2.4(b) shows an alternative peak detector circuit using operational amplifiers (op-amps). The first op-amp provides the high input impedance for the input from the detector. As in the previous circuit, the capacitor will charge as the input voltage increases, and the diode will not permit the capacitor to discharge when input falls.

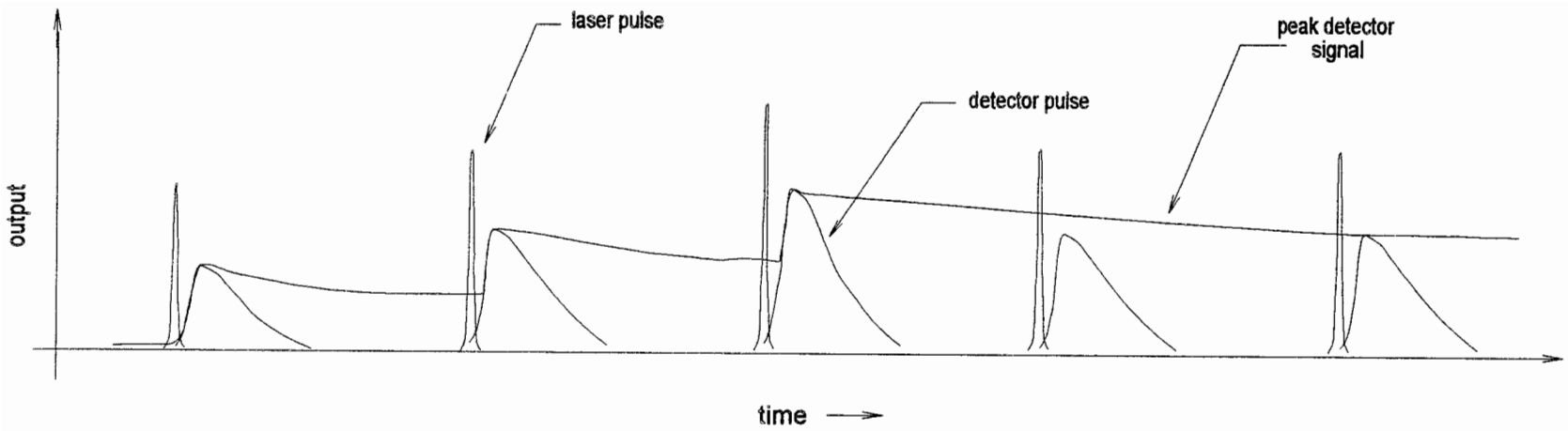

Figure 2.3. The peak detector circuit follows the peaks of the pulses at the detector output. The optical pulses are not to scale, but shown to demonstrate the spreading of the pulse by the detector.

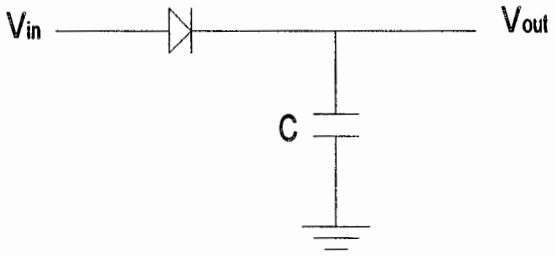

(a)

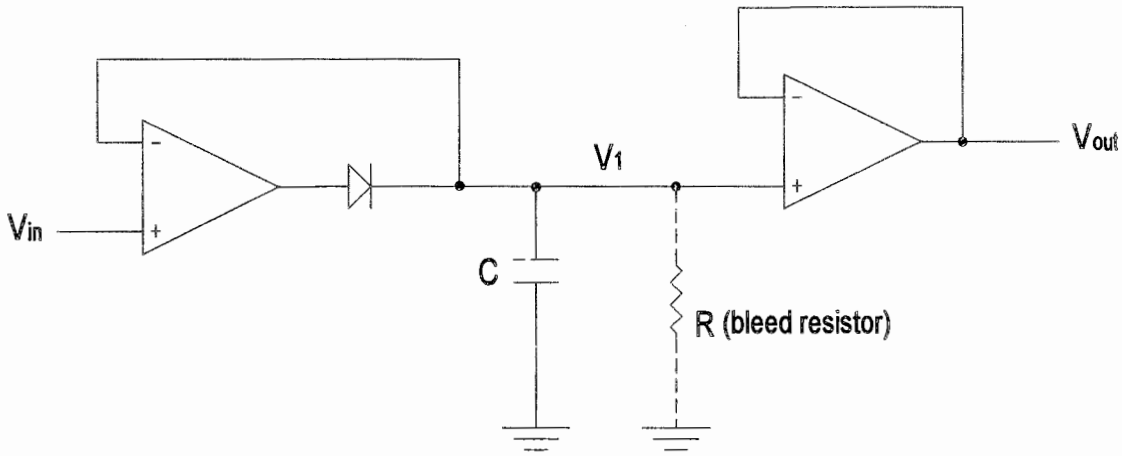

(b)

Figure 2.4. Two circuit alternatives for peak detecting.

However, by taking feedback from V_1, the circuit is no longer limited by the diode drop. The second op-amp is configured as a voltage follower and works as a buffer, giving the circuit a low output impedance. This op-amp also presents a high impedance to the capacitor to prevent the capacitor from quickly discharging. Assuming an infinite impedance for the second op-amp, the rate at which the capacitor does discharge (droop rate) is represented as $dV/dt = I_B/C$, where I_B is the input bias current of the first op-amp. The limiting slew rate of the circuit is defined as $dV/dt = I_{out}/C$, where I_{out} is the maximum output current of the op-amp. Therefore, selection of a value for C becomes a tradeoff in designing for a sufficiently slow droop rate and fast slew rate.

To achieve the design objectives for slew rate and droop rate, the proper circuit components must be chosen. FET op-amps typically have very low input bias currents and very high input impedances. The OPA606 is rated for 8 pA and 10^{13} Ω, respectively. In choosing a capacitor, the low leakage type (like polypropylene or polystyrene) would help reduce droop. In order to meet the droop rate requirement of 2 V/s, a value of C would need to be very small, on the order of pF. Tests on this circuit with various capacitance values led to the conclusion that this design would not work without the addition of a bleed resistor, R. This bleed resistor was an important step in the design, because it changes the droop rate dependence from a function of I_B/C to a time constant, 1/RC. Therefore, practical values for R and C could be chosen that meet the droop rate and slew rate design objectives [Jung, 1974]. This is, in fact, what was done for the final design of the circuit.

2.4. Final Design

The final design of the energy monitor includes the opto-mechanical parts and the electro-optical circuitry. Figure 2.5 details the dimensions and arrangement of the scattering block, filter assemblies, and base plate, and Figure 2.6 gives a picture of the completed energy monitor. They fit together to form a compact, self-contained unit that can be easily removed or placed in a different system. In the scattering block and filter assemblies, teflon spacers hold the optics in place and protect them from scratches. The

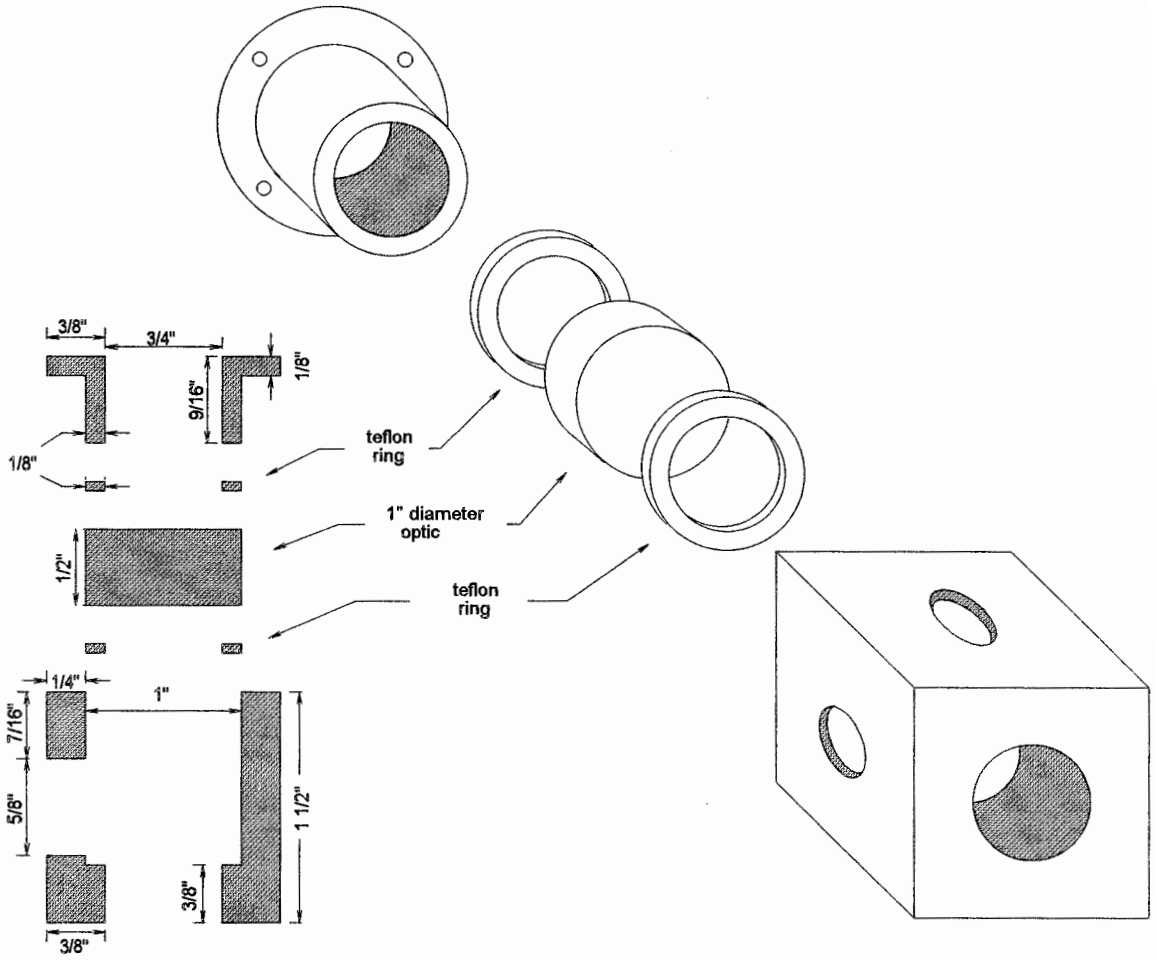

Figure 2.5(a). Energy monitor scattering block design.

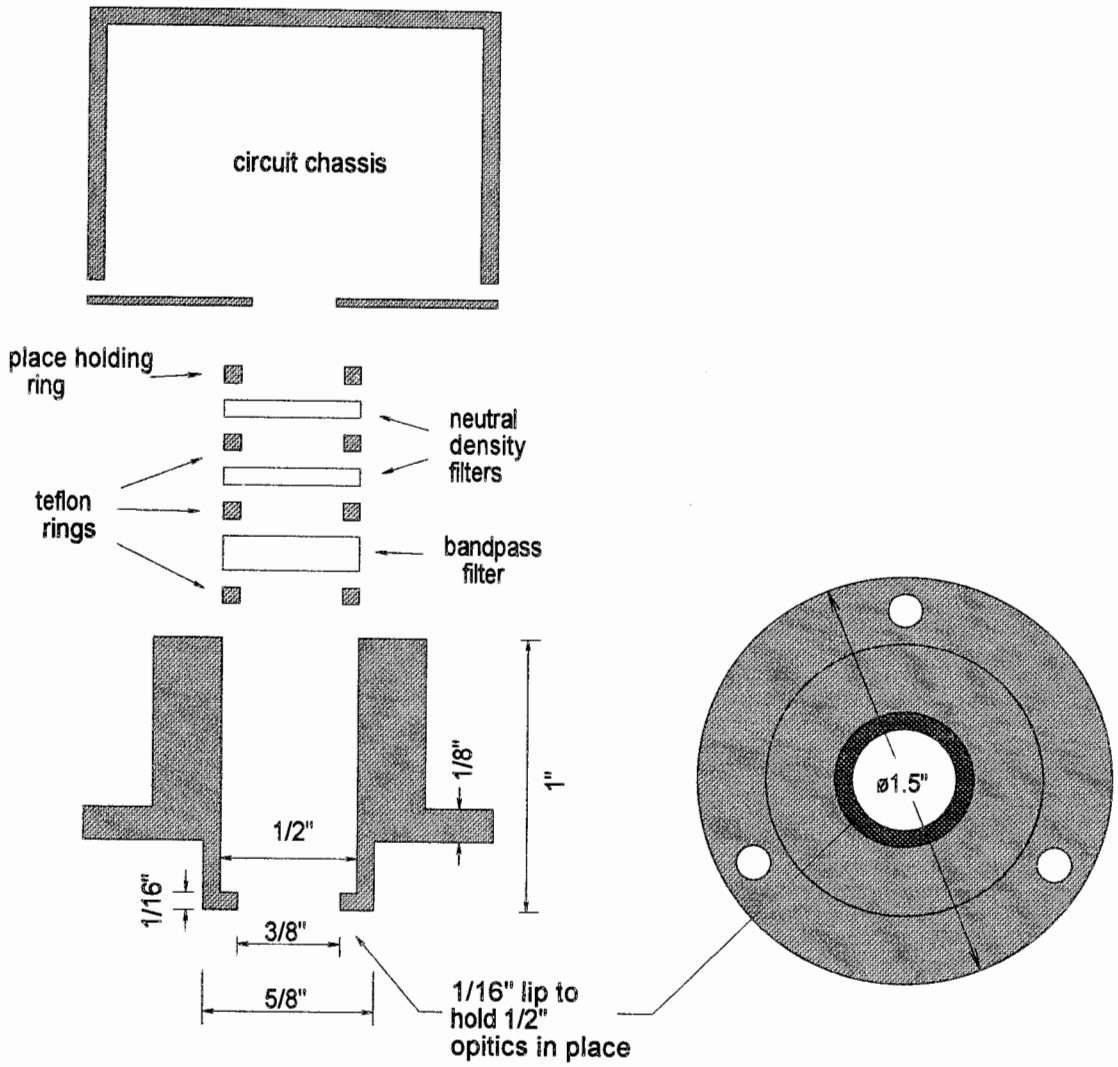

Figure 2.5(b). Energy monitor filter assembly design.

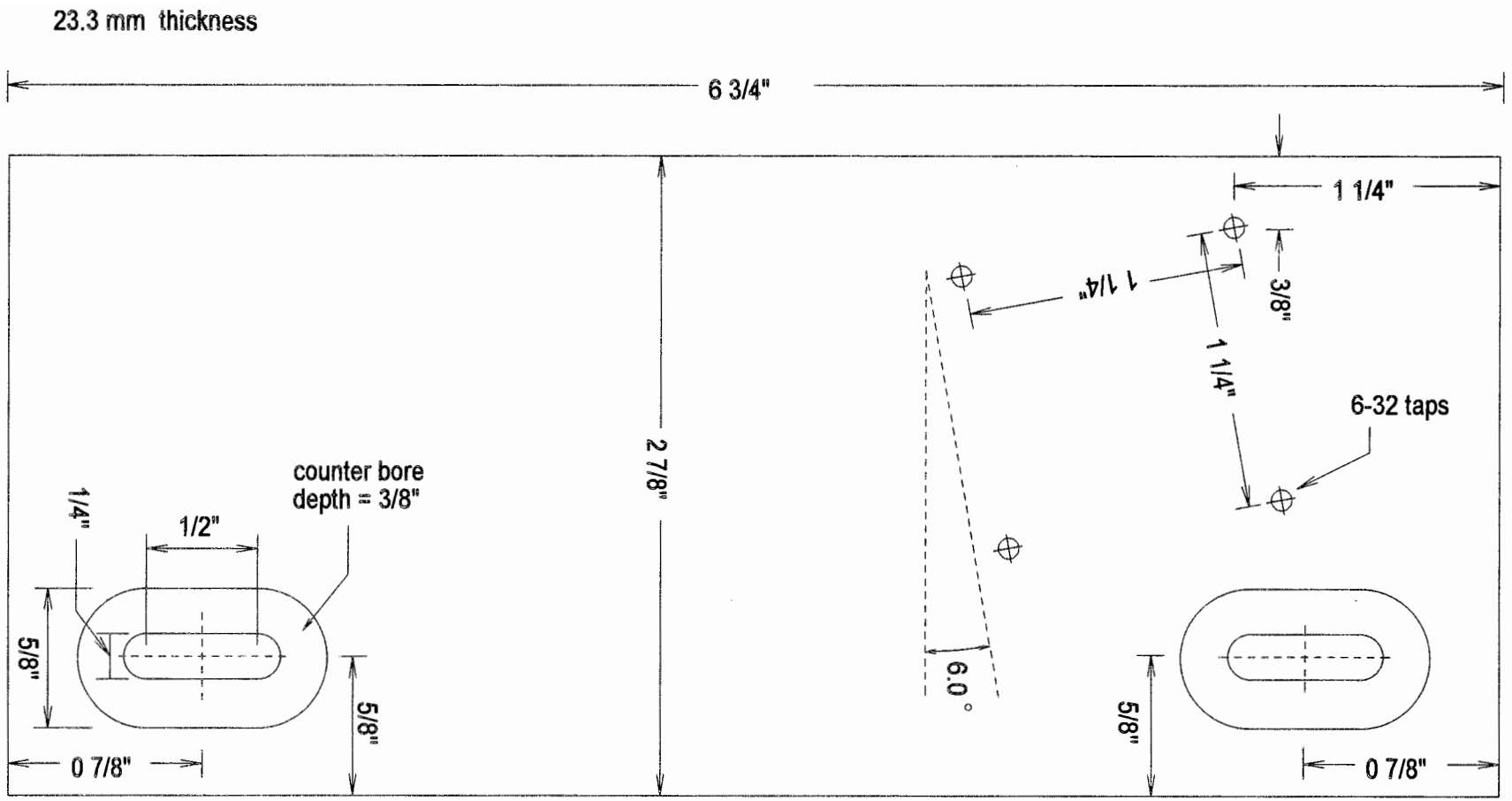

Figure 2.5(c). Energy monitor base plate design.

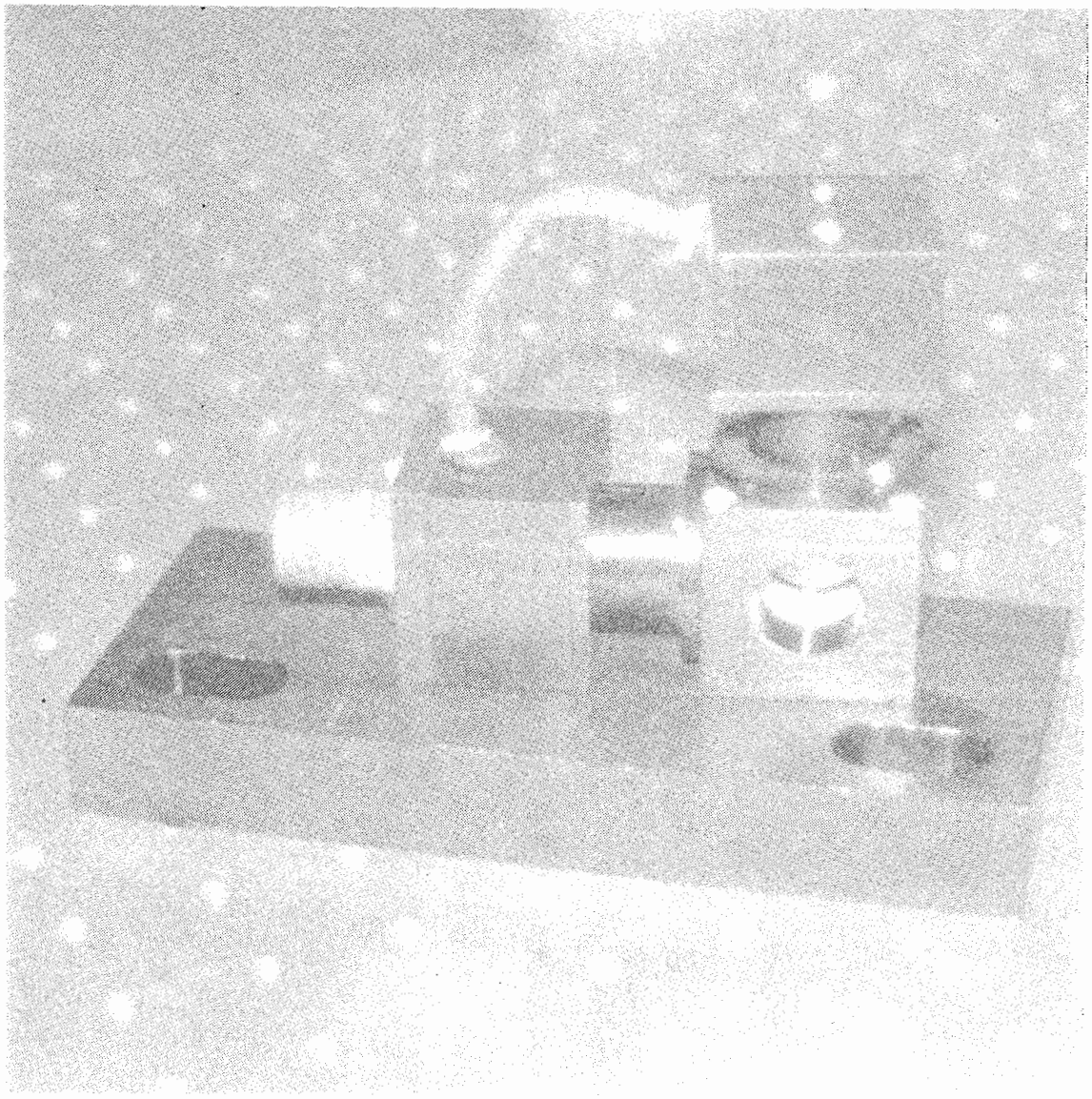

Figure 2.6. Picture of final energy monitor, including base plate, scattering block, filter assemblies, and detector boxes (532 channel on the side and 266 channel on top). For the convenience of using only one connector, the power and signal wires for the 266 detector box are fed through the 532 detector box.

base plate mounts to the optical bench of the laser system and places the center of the scattering window at the precise height of the beam. The detector chassis houses the detector and peak detector circuit. A connector attaches to this chassis and connects the circuit to the deck unit computer.

Figure 2.7 shows the final peak detector circuit diagram with the HUV-1100BQ detector. It is fundamentally the same as the circuit introduced in Figure 2.4(b). The 1N914 is also a low leakage diode, and the 0.047 μF capacitor is a polystyrene type capacitor. The 50 pF capacitor and 10 kΩ resistors were added to optimize stability and settling time. Also, low pass filters were added to the power supplies of each op-amp. With a 6 ns laser pulses as a source, this circuit's output successfully reaches the peaks and droops at a rate roughly equal to 2 V/s (although it is an exponential decay). The circuit followed the peaks from a maximum at 9 V down to 50 mV, the linear output range. Appendix B includes the printed circuit board design and a picture of the completed circuit board. Appendix C shows how the same board is used as a detector in another part of the LAPS system.

Although the choice of optics was governed largely by cost, the final set of optics used comprise the most expensive part of the entire energy monitor. The most important piece was the scattering window, mentioned previously. Initially, the design called for a double-V coating, optimized for 532 nm and 266nm. This coating offered the least reflectance at those two wavelengths, but resulted in large reflectance in other parts of the spectrum (like 1064 nm, or the third harmonic at 355 nm). Ultimately, however, the high intensity of the LAPS laser burned these coatings. They were replaced with broadband MgF_2 coatings. In addition to the proven strength of the MgF_2 coatings, the broadband design allows the optic to be used at other wavelengths. The bandpass filters were chosen with large bandwidths to minimize cost, since the energy monitor is a light-tight assembly with only the harmonic wavelengths present. The neutral density filters were also individually inexpensive, but the testing phase of the energy monitor a variety of combinations.

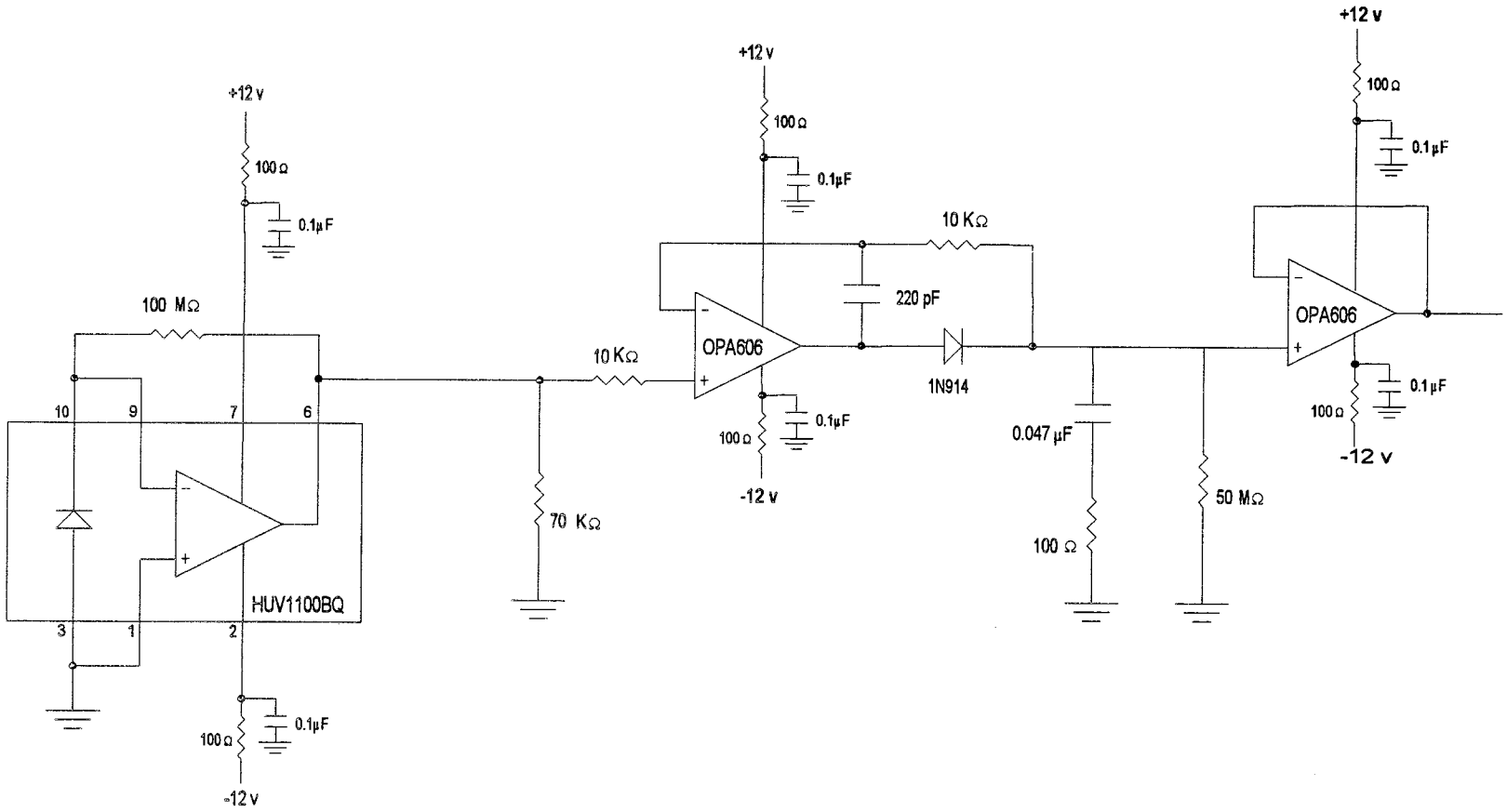

Figure 2.7. Peak detector circuit design.

The final test of the energy monitor is a calibration of its output against a factory calibrated power meter. The value of the monitor's output voltage does not need to match the power values but simply relate to the power meter linearly. Figure 2.8 includes data taken from the energy monitor and power meter at the 532 nm wavelength. A least squares fit illustrates the linearity of the energy monitor. Figure 2.9 is a similar calibration curve for the 266 nm wavelength. Both calibration curves yield values for slope and intercept that were incorporated into the computer software for an output in mJ. The energy monitor values, taken from the LAPS computer screen, exhibited a bounce which accounts for much of the error. The bounce comes from the shot-to-shot instability of the laser itself. Simply averaging the signal in the computer can slow the response of the energy monitor to reduce the bounce and look more like a power meter's response.

Despite the successful results, the design of the energy monitor is not complete without taking into consideration its effect on the larger laser and lidar systems. If the two surfaces of the scattering window were ideally non-reflecting, then the scattering window could be placed perpendicular to beam for an angle of incidence of 0°. With that orientation, however, the 0.5% to 1.5% reflectance on each surface would send enough energy back downstream into the optics of the laser, that damage to the laser would result. Therefore, drilled taps on the base plate in Figure 2.5(c) indicate that the window is oriented for a 6° angle of incidence (θ_i). Figure 2.10 shows the refractive effect on the beam as it passes through the window is a simple displacement of the beam. The refraction is governed by Snell's law,

$$n_i \sin(\theta_i) = n_t \sin(\theta_t). \tag{2-10}$$

At the front surface of the window, $n_i \approx 1$ for air and n_t is the refractive index of the glass. Applying Snell's law then to the back surface also, the displacement becomes,

$$displacement = (12.7mm)\left(\frac{\sin(\theta_i - \theta_t)}{\cos(\theta_t)}\right). \tag{2-11}$$

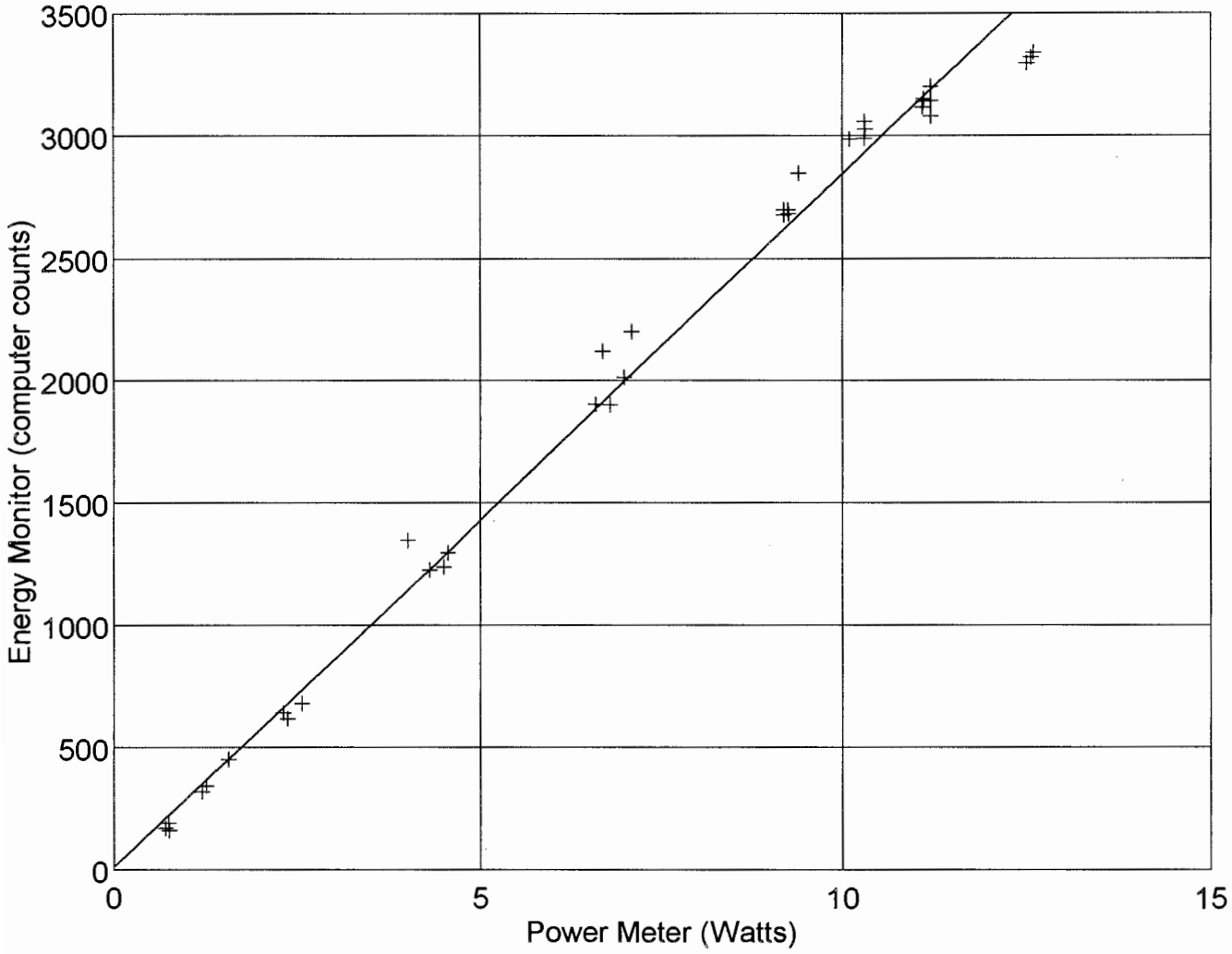

Figure 2.8. Calibration of energy monitor versus power meter at 532 nm.

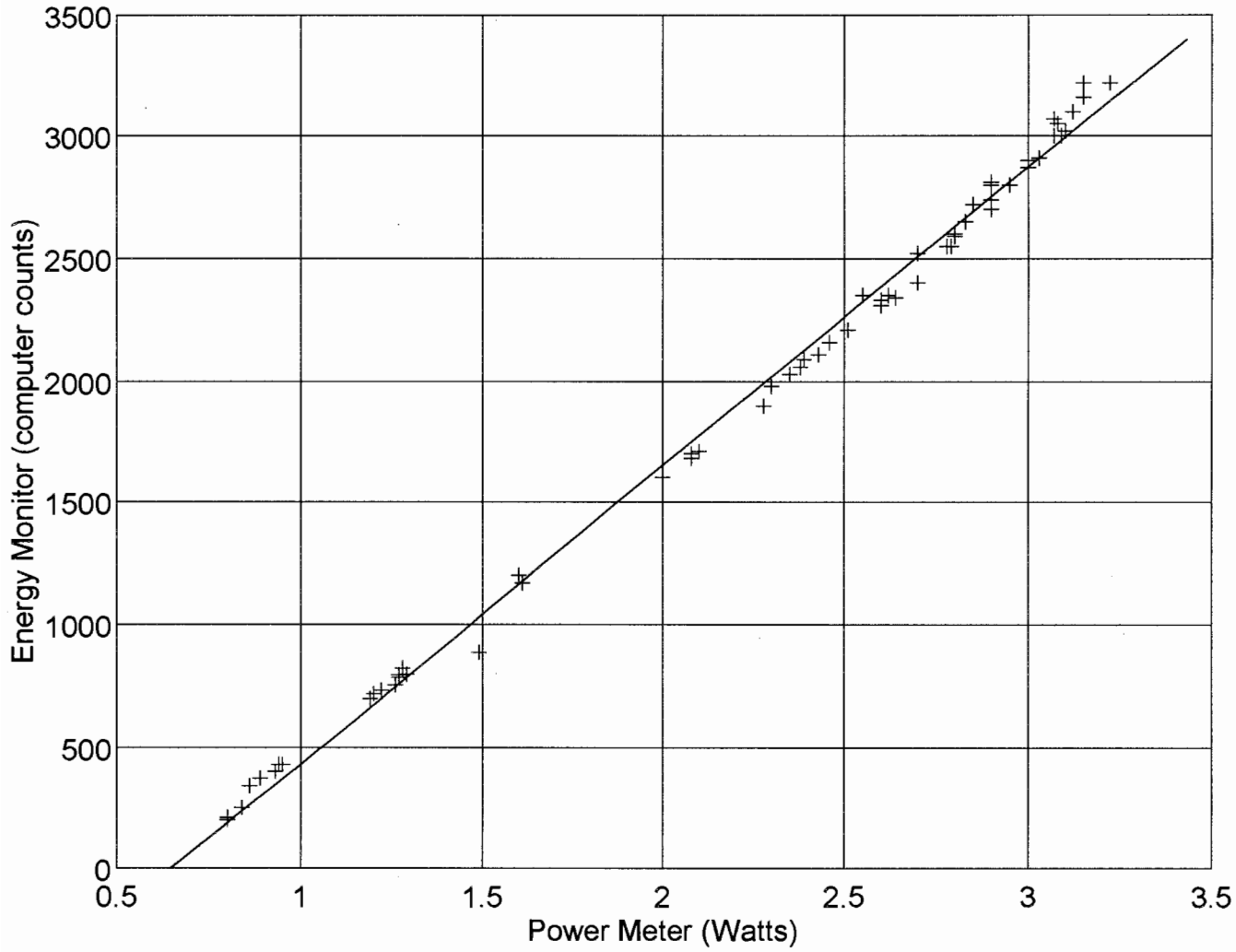

Figure 2.9. Calibration of energy monitor versus power meter at 266 nm.

Dispersion in the glass will define the index of refraction as a function of wavelength. The glass material is UV grade synthetic fused silica for which n = 1.49968 at 266 nm and n = 1.46071 at 532 nm. Therefore, the window will displace the beam at 266 nm more than it displaces the beam at 532 nm. Such a difference in displacement is undesirable for the beam expander following the energy monitor in the LAPS system. However, the actual difference for a 6° angle of incidence is 23.6 μm, which was determined to be negligible.

Just as the final energy monitor changed slightly from the initial design before testing, slight modifications are suggested for future energy monitors to be built. The size of the scattering block does not need to be so large. For example, a block that has less depth would make it easier to clean the window surfaces. A 1/8" lip holds the window in the scattering block, but a 1/16" lip would give the beam more room to pass through the block. The filter assembly does not need to be tubular shape with a flange, but a rectangular block with a ½" hole drilled in the middle would be easier to make and would fit with other parts better. The detector chassis should have a little more depth to give the circuit more headroom. Finally, a dual op-amp (OPA2107) could replace the two op-amps used on the circuit board.

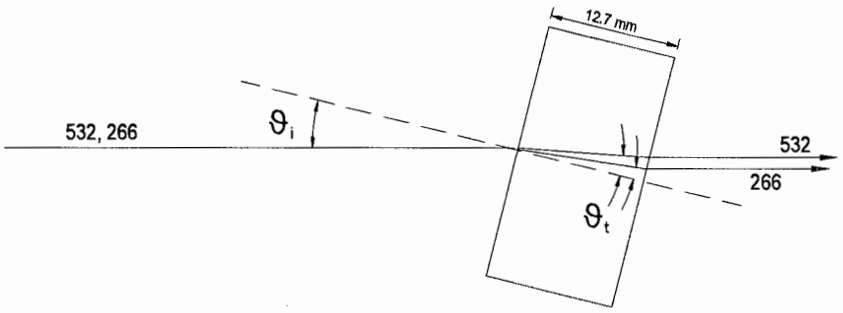

Figure 2.10. Displacement of beam in ½" optic at both 532 nm and 266 nm.

In conclusion, the energy monitor was born out of the need for a continuous measure of the laser's power at two harmonic wavelengths. Scattering out the edge of a glass window proved to be a practical method for obtaining a constant fraction of the laser's power. The resulting assembly built around the scattering window was simple and compact. The peak detector circuit performed linearly for a wide range of laser power. Final calibration curves verified the linearity of the entire energy monitor. The final product worked well for the LAPS laser system, and it could also work for other laser systems given a few minor adjustments.

Chapter 3

TUNING OF NONLINEAR CRYSTALS

3.1. Nonlinear Optics

The interaction of light and matter demonstrates the common effects of reflection, refraction, absorption, and scattering. These effects respond linearly to optical field intensity, and they do not alter the frequency of the incident radiation. It was not until the 1960's, with the advent of lasers, that optical nonlinear phenomena began to unfold. The extensive research emerged from the first observation of an optical frequency twice that of the incident laser beam as the beam passed through a quartz crystal [Higgens, 1994]. Now, a variety of nonlinear optical effects have found practical application in nearly all electro-optical technologies.

One can describe the nonlinear interaction of light and matter in a variety of ways. Fundamentally, it can be viewed as intense light changing the properties of an optical material which then acts on the light itself in a nonlinear manner. In this case the induced polarization **P** is not *linearly* dependent on the incident electric field **E**. A formula for the *linear* relationship between the two is,

$$P_L(\omega) = \epsilon_0 \, \chi(\omega) \, E, \tag{3-1}$$

where χ is the dielectric susceptibility. However, this relationship can be expanded in an infinite Taylor series, so the more general case is,

$$P(\omega) = \epsilon_0 \, [\chi_1(\omega) \, E + \chi_2(\omega) \, EE + \chi_3(\omega) \, EEE + \ldots], \tag{3-2}$$

where χ_1 is the linear, first-order susceptibility at low optical intensities. The higher order terms constitute the nonlinear dependence on the field such that,

$$P = P_L + P_{NL}. \tag{3-3}$$

The second-order susceptibility χ_2, when P ~ EE, accounts for a generated beam with

twice the frequency of the fundamental frequency ω at the input. The third-order susceptibility χ_3 explains the mixing of two incident fields at ω_1 and ω_2 where the output has components at ω_1, ω_2, and at $\omega_3 = \omega_1 \pm \omega_2$. This is the basis for second- and third-harmonic generation.

3.1.1. Harmonic Generation

Although a large variety of lasers have been demonstrated in the lab, only a handful are commercially practical, and most of these lasers operate at only one or a few frequencies. Harmonic generation, therefore, significantly increases the number of available frequencies, and this technique has proven itself useful in almost all areas of the electro-optic industry. A clear understanding of harmonic generation can teach us how to best exploit and control its properties. The mathematical development of the second-harmonic generation will reveal some of these properties.

The following mathematical development follows the standard text development such as Yariv [1971] and Milloni [1988]. It starts with the laser beam represented by an oscillatory electric field,

$$\mathscr{E}(t) = Re(E_\omega e^{-i\omega t}) = \tfrac{1}{2}\,(E_\omega e^{-i\omega t} + E_\omega^* e^{i\omega t}). \tag{3-4}$$

Next, assume that both the incident and second-harmonic fields propagate in the *z*-direction as monochromatic plane waves. The electric field for the second-harmonic is now,

$$\mathscr{E} = \tfrac{1}{2}\left[E_{2\omega} e^{-i(2\omega t - k_{2\omega} z)} + E_{2\omega}^* e^{i(2\omega t - k_{2\omega} z)}\right]. \tag{3-5}$$

As already stated, the second-order nonlinearity, denoted by $P_{NL} = \epsilon_0 \chi_2 EE$, contributes the above second-harmonic field to the output. Now, applying Maxwell's equation to the generated field,

$$\nabla^2 \mathscr{E} - \epsilon_0 \mu_0 \frac{\partial^2 \mathscr{E}}{\partial t^2} = \mu_0 \frac{\partial^2 P_{NL}}{\partial t^2} , \tag{3-6}$$

yields the simple differential equation,

$$\frac{dE_{2\omega}}{dz} = i\omega \sqrt{\mu_0/\epsilon_{2\omega}}\ \epsilon_0 \chi_2 E_\omega^2(z)\ e^{i\Delta kz} , \tag{3-7}$$

where,

$$\Delta k = 2k_\omega - k_{2\omega} = 2\omega\sqrt{\mu_0\epsilon_0}\ [n(\omega) - n(2\omega)] . \tag{3-8}$$

If we assume that very little of the incident electric field is attenuated, so that $E_\omega(z) \approx E_\omega(0)$, then the solution to (3-7) becomes,

$$|E_{2\omega}(L)|^2 = \frac{\mu_0 \omega^2 (\epsilon_0 \chi_2)^2}{\epsilon_{2\omega}} |E_\omega(0)|^4 \left(\frac{\sin \tfrac{1}{2}\Delta kL}{\tfrac{1}{2}\Delta kL} \right)^2 . \tag{3-9}$$

A physical, measurable quantity is the time-averaged intensity. For the incident and generated electric fields,

$$I_\omega = \tfrac{1}{2} \sqrt{\epsilon_\omega/\mu_0}\ |E_\omega| , \qquad I_{2\omega} = \tfrac{1}{2} \sqrt{\epsilon_{2\omega}/\mu_0}\ |E_{2\omega}| . \tag{3-10}$$

Equations (3-9) and (3-10) lead to an important result: the intensity of the generated light at the second-harmonic frequency is proportional to the square of the incident intensity. That is equivalent to saying that an increase in the power density of the incident beam in a nonlinear crystal significantly increases the power generated at the harmonic frequency. In most applications the beam makes a single pass through a nonlinear crystal which is outside the laser cavity, but there are additional configurations that increase the power generated at the harmonic frequency. For example, a focused beam will increase the power density, thereby increasing the conversion efficiency. Another way to increase the power density in the crystal is to place the crystal either inside a laser cavity or inside

another resonator [Hecht, 1992].

Making note of the relationship $n^2(\omega) = \epsilon_\omega/\epsilon_0$, the power conversion efficiency becomes,

$$eff. = \frac{I_{2\omega}(L)}{I_\omega(0)} = 2\left(\frac{\mu_0}{\epsilon_0}\right)^{3/2} \frac{\omega^2 (\epsilon_0 \chi_2)^2}{n^2(\omega)\, n(2\omega)} I_\omega(0)\, L^2 \left(\frac{\sin \tfrac{1}{2}\Delta kL}{\tfrac{1}{2}\Delta kL}\right)^2. \qquad (3\text{-}11)$$

An important conclusion from this relationship is that the efficiency is reduced by a factor of $\sin^2(x)/x^2$ where x varies with Δk. Figure 3.1 shows the shape of an ideal $\sin^2(x)/x^2$ or sinc^2 function. From (3-8), Δk depends on the difference between the indices of refraction at ω and 2ω. Therefore, with $v = c/n$, the difference becomes a phase-velocity mismatch. The conversion efficiency goes to a maximum as Δk approaches 0, where the system is said to be "phase-matched" and the two waves add constructively.

One method of phase-matching exploits the natural birefringence of anisotropic crystals [Yariv, 1971]. Such a crystal could have two orthogonal polarization eigenmodes, called the ordinary wave and the extraordinary wave. The refractive index

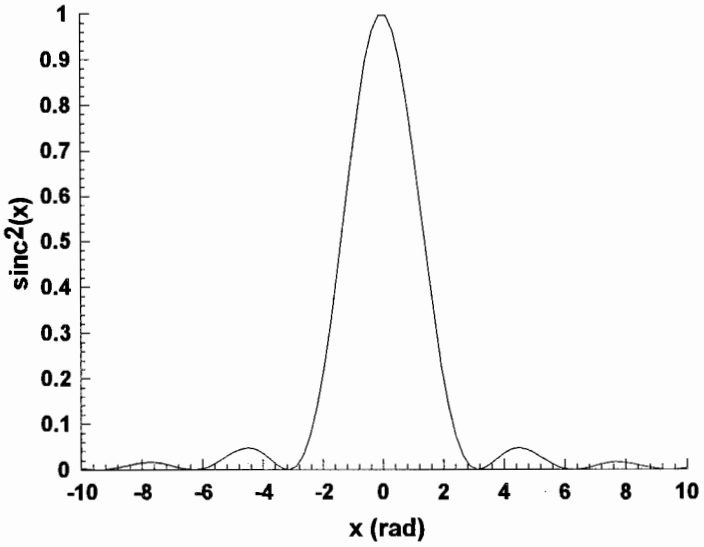

Figure 3.1. $\text{Sinc}^2(x)$ function.

for the ordinary wave is denoted by n_o and remains a constant for a given θ. The refractive index n_e of the extraordinary wave depends on the its propagation angle relative to the optical axis of the crystal. Figure 3.2 shows that the phase-matching condition is met where,

$$n_e^{2\omega}(\theta_m) = n_o^{\omega}. \tag{3-12}$$

The angle θ_m is the optimal power conversion angle. Practically, it may be a very difficult condition to accomplish. Very precise angle adjustments to the crystal optimize its conversion efficiency for a given input power level. However, this angle-tuning method still is the most common method in commercial laser systems today, and it is the method that the LAPS laser uses.

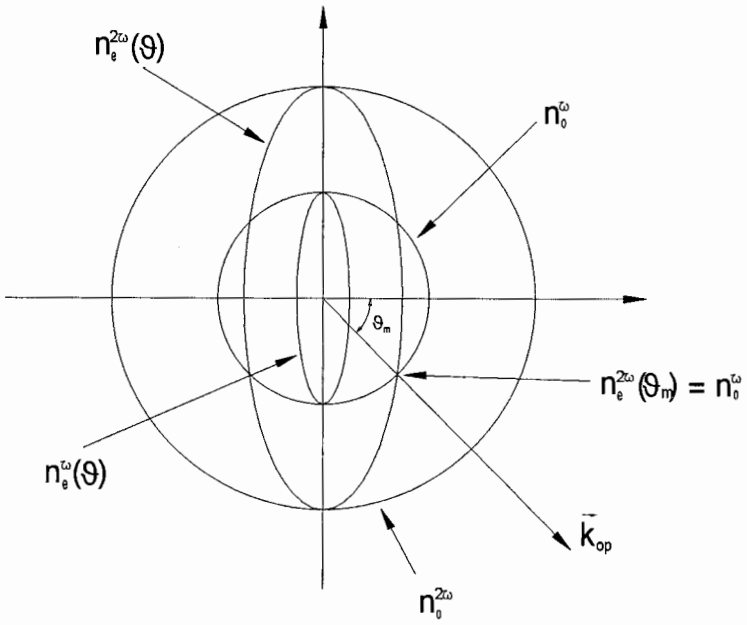

Figure 3.2. Phase matching condition.

3.1.2. Application

It is now time to apply the preceding development to an actual laser and harmonic generating crystals. Again, the laser's fundamental wavelength is 1064 nm, and at that wavelength it produces 1.6 Joules/pulse with a pulse duration of 7 ns. For a beam diameter of 9.5 mm, the intensity of a single pulse becomes about 460 MW/cm^2. The beam passes through the second-harmonic generator (SHG) to produce green light at 532 nm, and then it passes through the fourth-harmonic generator (FHG) to produce UV radiation at 266 nm. The SHG uses KH_2PO_4 (KDP) for its nonlinear crystal. The FHG uses either KD_2PO_4 (KD*P) or a more efficient β-BaB_2O_4 (BBO) crystal. Both harmonic generators are angle-tuned for peak power conversion efficiency by a precise micro-positioner. Figure 3.3 shows the angle dependence of the power conversion efficiency in this laser system for the SHG. It approximately agrees with the $\sin^2(x)/x^2$ factor in Equation (2-9). When the SHG is falls off its peak during operation, the FHG's conversion suffers dramatically. This observation also agrees with the $I_{2\omega} \sim (I_\omega)^2$ dependence in Equation (2-9).

Of the various crystals used in harmonic generation, KDP is the most common. There are other crystals that perform better than KDP in terms of % conversion, damage threshold, thermal conductivity, and transparent range. However, the KDP crystals can easily be grown to large sizes and with great purity. Table 3.1 shows the appropriate indices of refraction at ω, 2ω, and 4ω taken from [Fejer, 1994].

Table 3.1 Indices of refraction for KDP

	1064 nm	532 nm	266 nm
n_o	1.49419	1.51108	1.57177
n_e	1.46028	1.46962	1.52051

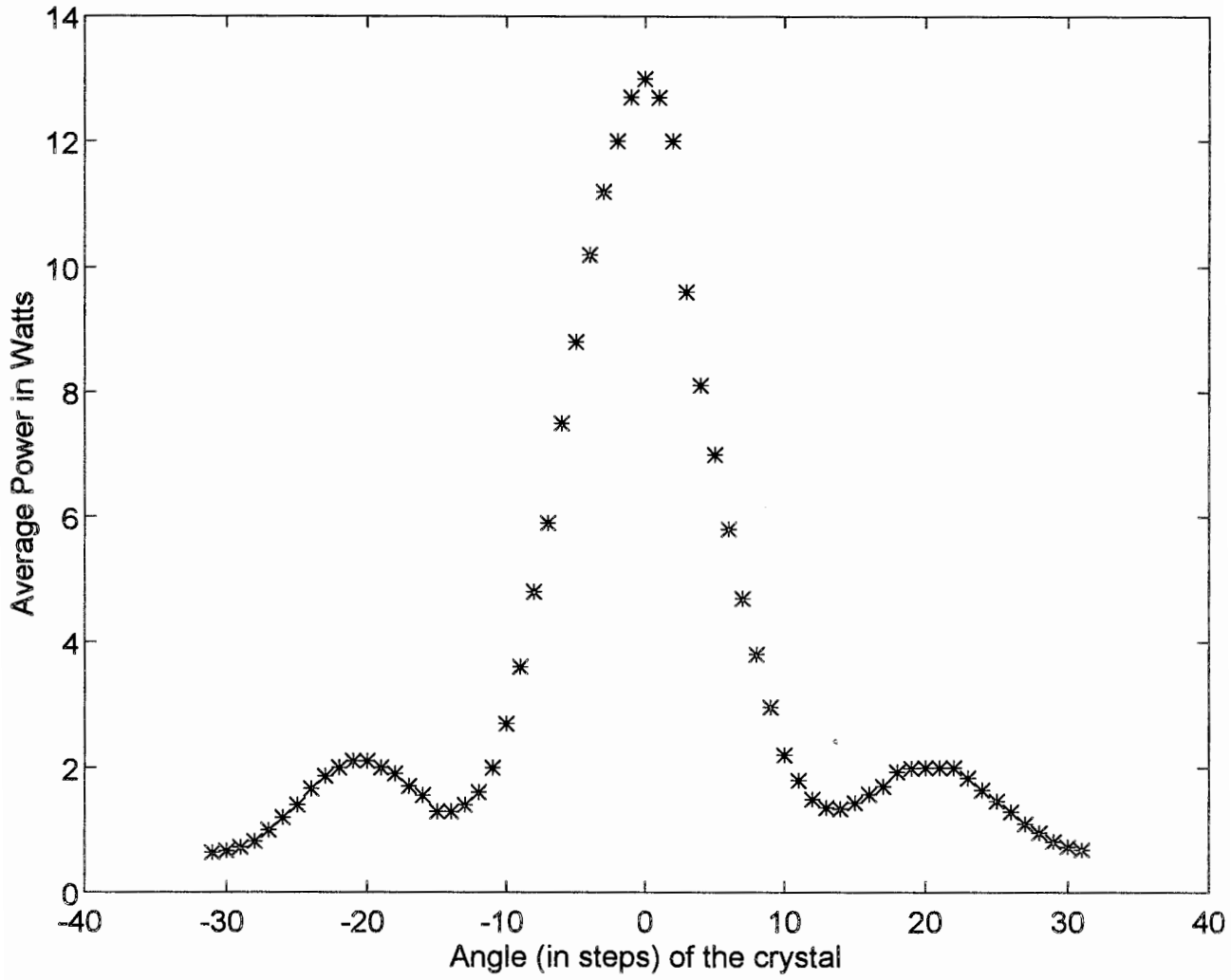

Figure 3.3. Angular dependence of SHG efficiency. Each step corresponds to about 0.1° of angular rotation. Data taken on 12/8/94.

To solve for θ_m, [Khoo, 1994] gives the following relationship,

$$\sin^2\theta_m = \frac{(n_o^{\omega})^{-2} - (n_o^{2\omega})^{-2}}{(n_e^{2\omega})^{-2} - (n_o^{2\omega})^{-2}} . \tag{3-13}$$

For the KDP crystal in the SHG, θ_m is 39°. The laser vendor finds the crystal's optical axis and then cuts and positions the crystal accordingly. As a sidenote, the harmonic generating units should include one additional feature which has been assumed up to this point. The indices of refraction in the crystal will change with temperature, so the crystal is maintained at an elevated temperature that remains stable and relatively independent of both heat from the laser beam passing through the crystal and temperature changes from the local environment.

Although the classical solution derived in Section 3.1.1 yields some important results, the full quantum mechanical approach defines a new nonlinear coefficient which is more common in tables of nonlinear crystal properties. The following equation, when compared to (3-2), shows that $\bar{d}$ is nothing more than a different notation for the susceptibility,

$$P_{2\omega} = \bar{d}\, E_{\omega}^2(z) . \tag{3-14}$$

However, $\bar{d}$ is written as a tensor with 3 x 6 matrix elements that indicate the crystal structure and its capacity to generate harmonics. From a table of nonlinear crystals, the $\bar{d}$ tensor for KDP is of the form,

$$\begin{pmatrix} 0 & 0 & 0 & d_{14} & 0 & 0 \\ 0 & 0 & 0 & 0 & d_{14} & 0 \\ 0 & 0 & 0 & 0 & 0 & d_{36} \end{pmatrix} . \tag{3-15}$$

However, the only nonlinear coefficient of any consequence is the d_{36} element, due to the structure and orientation of the crystal. KDP is a lossy medium, so the value for d_{36}

depends on 2ω. Its value in the visible spectrum is about 6.3×10^{-24} (MKS units) [Yariv, 1984]. The crystal has a thickness of 25 mm.

Now, all the variables in (3-11) are defined, yet this equation, however useful in characterizing the conversion, yields an unrealistic efficiency. The reason for this comes from the assumption made earlier that the power at the fundamental frequency is not depleted. In the laser system described above, this is not a valid assumption since about 50% of the power at ω is lost in the conversion. Therefore, Yariv [1984] defines the conversion efficiency of second harmonic generation corrected for a depleted input. For a 25 mm thick sample of KDP, the efficiency is about 50%, which is what can be achieved in the LAPS laser system.

The fourth-harmonic generator (FHG) doubles the frequency of the 532 nm wavelength in the same manner as the SHG did to the fundamental 1064 nm wavelength. It can use a KD*P crystal of length 6 mm and generate 90 mJ/pulse for a conversion efficiency of about 11% into the UV. However, as an alternative to KD*P, the BBO crystal has a nonlinear coefficient of d_{22} which is about 4 times that of KD*P [Svelto, 1989]. So, for the same input intensity at 532 nm, this FHG will generate more power at the 266 nm wavelength than the KD*P could. The vendor expects to achieve 130 mJ/pulse at this wavelength for a conversion efficiency of about 16%. Furthermore, BBO inherently has a higher damage threshold than KD*P and many other harmonic generating crystals have. The difficulty in this case comes in growing pure BBO of a useful size.

After characterizing the nonlinear process of harmonic generation and giving an example, we again consider our application. Chapter 1 discussed how the LAPS lidar system required a powerful source in the visible and UV spectrum. The Nd:YAG laser is the choice for this application, but the fundamental frequency of 1064 nm is not used at all. In fact, the power at that wavelength is split from the output and dumped into a beam dump after it passes through the SHG. Therefore, nonlinear optics are necessary to transfer the power to wavelengths where it is needed. With second-order harmonic generation, the intensity at the generated wavelength will be proportional to the square of the incident intensity, regardless of the crystal used. Furthermore, the conversion

efficiency in an angle-tuned arrangement varies with the angle in a $(\sin^2 x)/x^2$ fashion. These conclusions lend themselves to a proper characterization of the physical system, which is the first step in designing an automated control routine.

3.2. Tuning

The tuning of a laser harmonic generators is often accomplished manually by a laser operator with limited knowledge of the system, because a manual keypad, as in the Continuum laser, allows for convenient trial-and-error adjustments. However, an automatic tuning system requires special control routines unique to the system. Knowledge of the tuning system goes beyond the characteristics of harmonic generation identified in the previous section. A computer subroutine can then account for the all the system's peculiarities.

The fundamental design objective of this subroutine is to tune each of the crystals reliably and efficiently. The subroutine must tune the SHG successfully before attempting to tune the FHG, because the conversion efficiency of the FHG depends on the square of its input power at 532 nm. Also, the subroutine must find the best conversion efficiency by avoiding the side lobes characteristic of the $\text{sinc}^2 x$ function. A simple gradient search could get locked onto a side lobe maximum and never fully tune the crystal. For the subroutine to operate reliably, it must account for the temperature stability of the crystals and the physical limits or end-stops of the micro-positioner. For the subroutine to operate efficiently, the search must incorporate an adaptive step size feature.

The complete control system includes four components: the energy monitor, deck unit computer, laser electronics, and harmonic generating units. The energy monitor serves as the sensor by providing the deck unit computer with power information at both harmonic frequencies. The computer makes a control decisions and sends that decision via an RS232 port to the laser electronics. The laser electronics then pulse the micro-positioner which rotates the crystal slightly. The control decision manifests itself as n steps clockwise or counterclockwise, but the laser responds to only one step at a time. Therefore, the computer will send a single hexadecimal number (representing CW or

CCW) n times until the crystal is in place for the next iteration. Each iteration must not be faster than the time response of the system. The time response of the system is defined as the time for the micro-positioners to move plus the time response of the energy monitor.

At the heart of the control program is the search algorithm, of which there are many choices. A simple gradient search switches directions when the new value for power is less than the previous power. However, this method may end on the maximum of a side lobe and miss the true maximum. Identifying the low power at that side lobe's peak, the search algorithm would begin again on either side of the side lobe. Alternatively, the computer could scan the range of angles, record the profile, and return to the maximum, but this method would take far too much time. A random search has the potential to find the true maximum more efficiently than scanning the whole range, but it is not practical for the micro-positioner to physically jump around randomly. An efficient algorithm would find the maximum in as few as steps at possible [Brooks, 1958].

One possible solution avoids the side lobes and includes an adaptive step size feature. In fact, the following design uses the adaptive step size to avoid the side lobes. The algorithm relates the step size to the current value of power in the equation,

$$step\ size = \left(\frac{maxpower}{power} \right)^{\alpha} \tag{3-16}$$

where *maxpower* is a constant equal to the power at the harmonic wavelength when the harmonic generator is tuned and α is the scaling factor. Figure 3.4 shows the relationship graphically with quantized steps and different scaling factors. The relatively simply relationship makes large changes when the crystal is far from the optimum angle and small changes when the crystal is almost tuned. If the output step size of Equation (3-16) for the power at the top of a side lobe is greater than half the width of the side lobe, then the algorithm will surely skip over the side lobe and find the main lobe and true maximum. For example, Figure 3.3 gives values for the side lobe maximum, true maximum, and the half width (in steps) of the side lobes. Putting these values into Equation (3-16) yields an α approximately equal to one. The value for α could be further increased for more

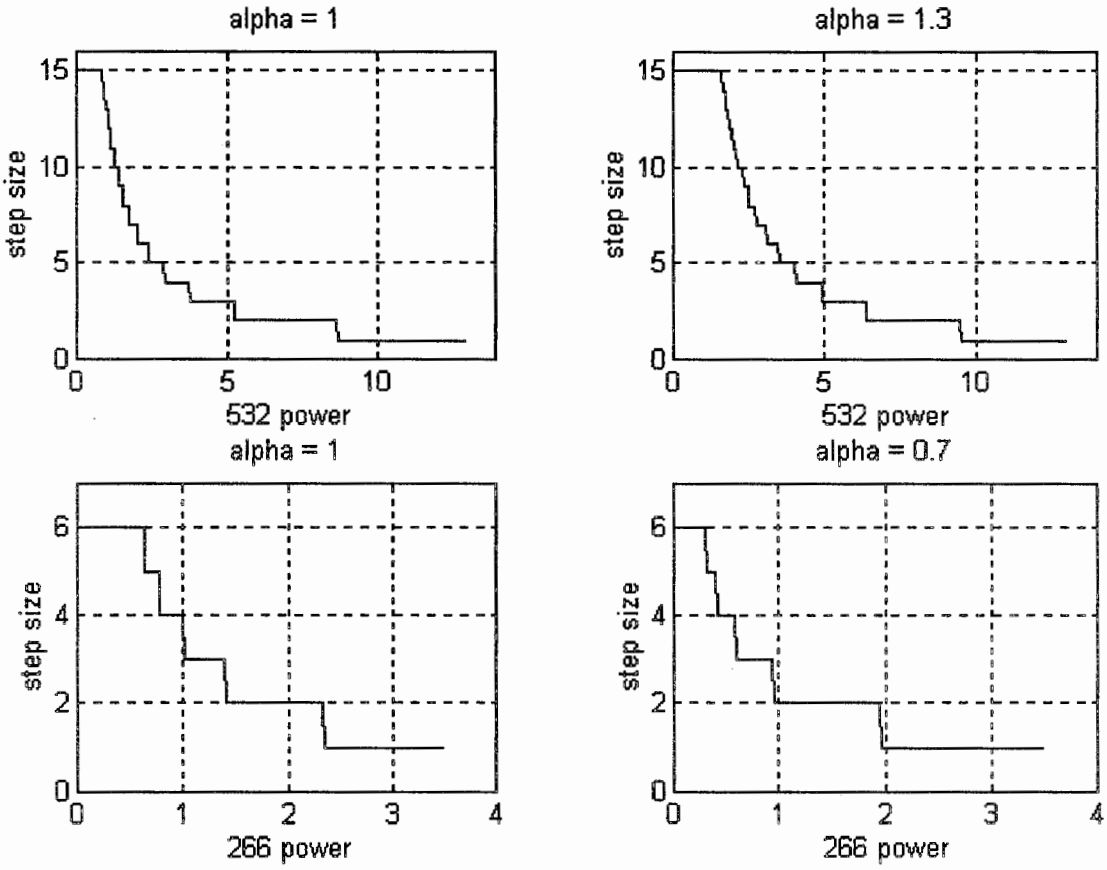

Figure 3.4. Step Size versus power for tuning algorithm. Different values for alpha (α) give the control different step size characteristics.

assurance that the algorithm would skip over side lobes. However, if α is too large, the algorithm could skip over the main lobe. For the example in Figure 3.3, the step size for a power of 1.5 W must be less than 26 steps or the full width of the main lobe. For the purposes of this thesis, the algorithm described above is called a modified gradient, adaptive step size algorithm.

The FHG exhibits a somewhat different behavior than the SHG, but the control is similar. The angle dependence of the FHG efficiency does not have noticeable side lobes, and the main lobe is narrower (in steps) than that of the SHG. Also, the position of peak conversion efficiency will tend to drift during the first several minutes of operation, unlike the SHG which has very good temperature stability almost from system startup. As a result of its differences to controlling the SHG, the FHG control algorithm will begin with a routine that sweeps (one or two steps at a time) the range of angles, then launches the modified gradient, adaptive step size algorithm as in the SHG control. A value for α will be less than the value used in the SHG control, because skipping over side lobes is not as critical, and the narrower main lobe is more sensitive to small steps. This program then needs to run until the peak conversion efficiency stabilizes and stops drifting.

The harmonic generators have a physical limitation in how far they can rotate the crystals. Reflections off the surfaces of the crystal could damage other components or optics in the laser if the angle goes beyond the end stops. The laser electronics return a hexadecimal string to the computer if the harmonic generator reaches an end stop. Both control algorithm responds to that by reversing the direction of the crystal rotation. In the case of the SHG, the power of the generated beam near the end stops would be low enough for that next step to move in large steps away from the end. The FHG control will not run into the end stops unless it is in the sweep mode, which will simply reverse its direction at that end stop.

A computer simulation of the control system minimizes actual use of the laser during the development and testing phase. The simulation adds insight to the control problem and saves the laser from ware and possible damage. Figure 3.5 is the simulation design in the software environment created by SIMULINK. The first step in creating the

simulation is defining the system. The look-up table represents the angle dependence of the SHG as in Figure 3.3. The input to that block is the angle (in steps) of the crystal, and the output is the corresponding power level. Like the energy monitor, this block sends laser power information to the computer. A control program in the computer outputs n number of steps clockwise ($n > 0$) or counterclockwise ($n < 0$). That number is fed back to a summer which adds the control output to the angle variable. The unit delay boxes ensure that one iteration begins with the detection of power and ends with the movement of the control decision. The simulation monitors different variables by displaying in the MATLAB workplace or on a graphical scope.

One additional block accounts for non-ideals in the system by adding noise. Remember that the micro-positioner is a not a stepper motor, but rather a pulsed DC motor. Therefore, the distance that each step moves the crystal is not a constant. Or, perhaps, the energy monitor records a voltage spike than does not fit to the curve in Figure 3.3. The single noise block approximately models these and other non-ideals by making quantized shifts in the angle.

Before the simulation, a variety of complicated control algorithms were theorized. The simulation helped refine the control algorithm to a very simple design that worked. The simulation results demonstrated that the modified gradient, adaptive step size algorithm consistently tuned the SHG, even in the presence of a large noise signal. Furthermore, the simulation results give an idea of how many iterations the control system will need in order to tune the SHG, given any initial starting position. An equivalent program for the FHG required some modifications, but the results were similar.

The tuning of the nonlinear crystals, in conclusion, began with the proper characterization of the system. A control algorithm evolved out of the system requirements and a simulation. The simulation confirmed the proper operation of the algorithm and continues to serve as a test bed for modifications to the control system. Appendix D includes a program listing of the subroutine that resides in the deck unit computer memory.

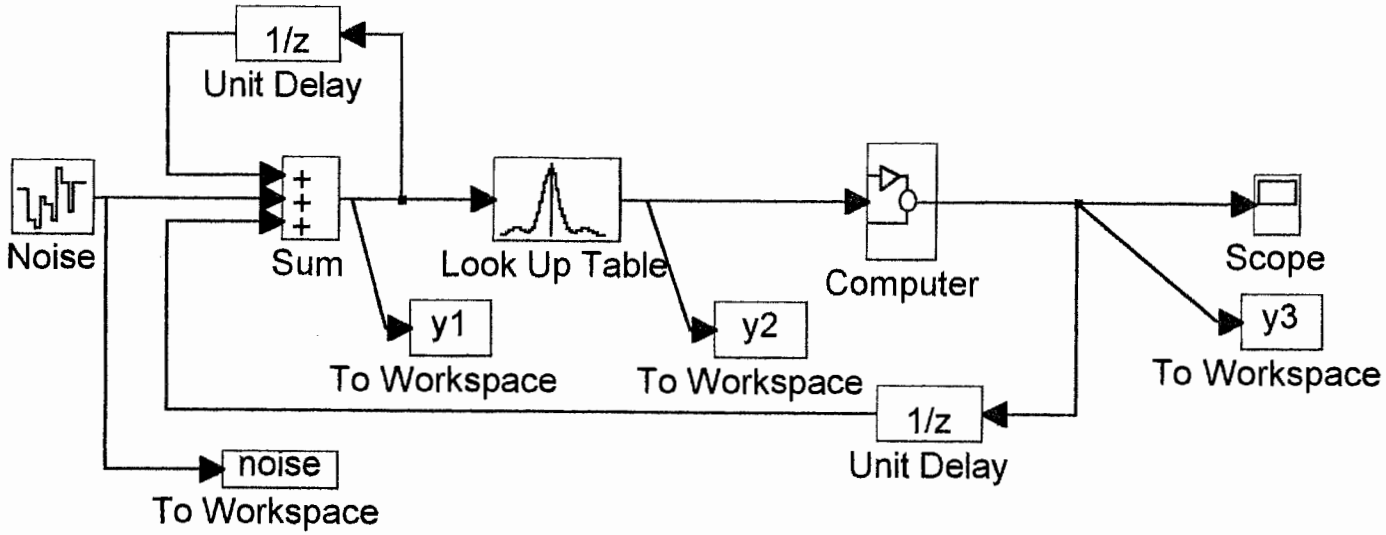

Figure 3.5. Simulation design in SIMULINK.

Chapter 4
CONCLUSION

This thesis has demonstrated the use of a new energy monitor to characterize and optimize the power of a laser in a lidar application. Both the energy monitor and crystal tuning subsystems were designed to meet the specific needs of the LAPS system. They were also designed to be flexible. Having met the needs of LAPS, the designs can now meet the needs of other laser systems in other applications. The idea of scattering out the edge of a window could apply to any laser with high enough power. The energy monitor assembly need only change to accommodate the size of the laser beam. The peak detector circuit could serve any pulsed laser system by adjusting the time constant (1/RC) for the pulse repetition rate. Finally, the basic approach to the crystal control design and its simulation could suggest methods of tuning other harmonic generators.

Table 4.1 lists several laser systems taken from Hecht [1992] with output powers strong enough to make the window scattering technique useful. They are all pulsed systems unless otherwise noted with continuous wave (CW). The second column lists the laser's operating wavelength(s). If the laser is tunable in a range of wavelengths, then the energy monitor's bandpass filter must have a broad bandwidth. The third column lists the harmonic frequencies of laser systems where harmonic generation is commercially practical.

Research and industry, alike, continually find new applications for high power lasers. This thesis attempts to simplify the use of such lasers by continually characterizing and automatically optimizing the laser's power output. Future laser systems could incorporate similar energy monitors that give a calibrated measure of the lasers' own power. The use of such a monitor would then allow the laser systems to automatically maintain peak conversion efficiencies in the harmonic generators.

Table 4.1 Summary of high power laser systems

type	λ (nm)	harmonic λ's (nm)
KrF excimer	248	
XeCl excimer	308	
Pulsed or CW dye	320-1000	
XeF excimer	351	
Ar ion CW	450-520	
Copper vapor	510, 578	
Gold vapor	628	
Kryton ion	647	
Ti-sapphire	680-1130	350-470, 235-300
Ruby	694	347
Alexandrite	720-800	360-400
Nd-YLF	1047, 1053	523
Nd-glass	1061	
Nd-YAG	1064	532, 355, 266

References

Brooks, S. H., "A Discussion of Random Methods for Seeking Maxima," Operations Research, vol. 6, pp. 244-251, 1958.

Evanisko, G. R. "Characterization of the WAVE-LARS Polarization Lidar Transmitter and Receiver," MS Thesis, The Pennsylvania State University, 1994.

Higgens, T. V., "Nonlinear Optical Effects Are Revolutionizing Electro-optics," Laser Focus World, August, 1994.

Hecht, J., *The Laser Guidebook*. New York: McGraw-Hill, 1992.

Jung, W. G., *IC Op-Amp Cookbook*. Indianapolis: Howard W. Sams & Co., 1974.

Khoo, I. C., *Liquid Crystals: Physical Properties and Nonlinear Optical Phenomena*. New York: John Wiley & Sons, 1994.

Machuga, D. W., "Daytime Performance of the Lamp Rayleigh/Raman Lidar System," MS Thesis, The Pennsylvania State University, 1993.

Measures, R.M., *Laser Remote Sensing*. New York: John Wiley & Sons, 1984.

Milonni, P.W. and J. H. Eberly, *Lasers*. New York: John Wiley & Sons, 1988.

Philbrick, C.R., "Raman lidar measurements of atmospheric properties," Proceedings SPIE, vol. 2222, pp. 922-941, 1994.

Schumer, M. A. and K. Steiglitz, "Adaptive Step Size Random Search," IEEE Transactions on Automated Control, vol. AC-13, no. 3, June 1968.

She, C. Y., "Remote measurements of atmospheric parameters: new applications of physics with lasers," Contemporary Physics, vol. 31, no. 4, 1990.

Svelto, O., *Principles of Lasers*. New York: Plenum Press, 1989.

Yariv, A., *Optical Electronics*. Philadelphia: Saunders College Publishing, 1971.

Yariv, A. and P. Yeh, *Optical Waves in Crystals*. New York: John Wiley & Sons, 1984.

Young, A. T., "Rayleigh Scattering," Applied Optics, vol. 20, no. 4, pp. 533-535, 1981.

Appendix A

HUV-1100BQ

HUV Series (1100BG; 1100BQ; 2000B; 4000B)

Features

- Built-in Low Noise Amplifier
- Groundable Case
- Shielded Amplifier
- Large Active Area
- Wide Spectral Range
- Oxide Passivated Structure

Operating Data and Specifications at 23°C
Typical Performance at 0 V Bias (Photodiode) and ±15 V (Amplifier)

Characteristic	HUV-1100BQ	HUV-2000B	HUV-4000B	Units
Active Area	5.1	23.4	100	Sq. mm
Spectral Range[1]	← 185-1150 →			nm
Responsivity at 900 nm	130	130	130	10^6 V/W; R_f = 200 Megohms
Responsivity at 254 nm	28	28	28	10^6 V/W; R_f = 200 Megohms
Responsivity at 200 nm	16	16	16	10^6 V/W; R_f = 200 Megohms
Frequency Response (-3dB)[3]	DC-1100	DC-1100	DC-1100	Hz
Noise Voltage at 20 Hz	4	9	9	10^{-6} V/Hz$^{1/2}$;
NEP (900,20,1)	0.03	0.07	0.07	10^{-12} W/Hz$^{1/2}$
NEP (254,20,1)	0.14	0.32	0.32	10^{-12} W/Hz$^{1/2}$
NEP (200,20,1)[2]	0.25	0.56	0.56	10^{-12} W/Hz$^{1/2}$
Open Loop Gain	2	4	4	10^5
Bias Current[4]	30	15	15	pA at 25°C
Offset Current	3	5	5	pA
Offset Voltage[5]	3	3	3	mV
Offset Voltage Drift	5	10	10	10^{-6} V/°C
Output Resistance	250	500	500	Ohms
Slew Rate	12	0.5	0.5	V/10-6S
Supply Voltage	±5 to ±18	±12 to ±18	±12 to ±18	Volts
Supply Current	5	2.2	2.2	mA at ±15 V
Power Consumption	150	30	30	mW at ±15 V
Operating Temperature	← 0 to 70 →			°C

Notes

1. Spectral range 185-1150 nm applies to units with BQ suffix, 250-1150 nm for units with BG suffix.
2. Does not apply to units with BG suffix.
3. Operational performance with the recommended feedback resistor value. Other feedback resistor values may be used but will modify system NEP and frequency response.
4. Doubles for every 10°C rise in temperature.
5. Adjustable to 0 V with external trim potentiometer.

Typical Spectral Response

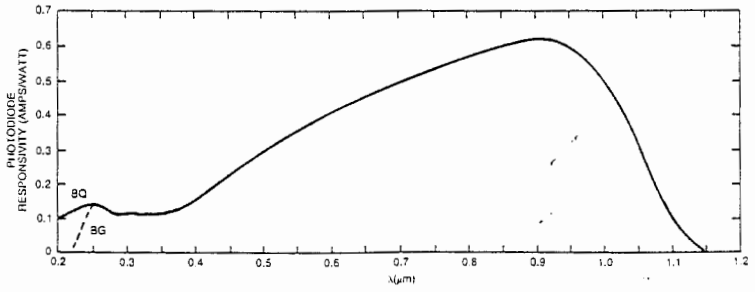

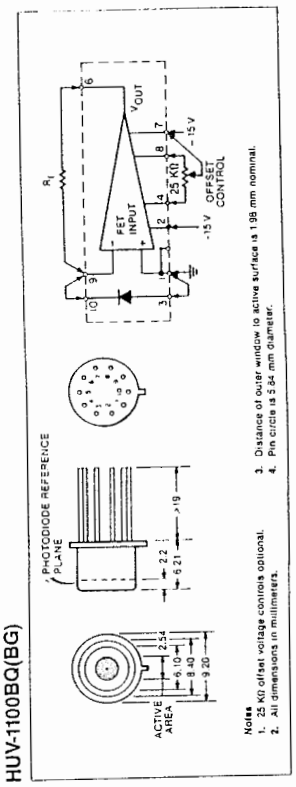

EG&G OPTOELECTRONICS CANADA

Appendix B

PRINTED CIRCUIT BOARD DESIGN

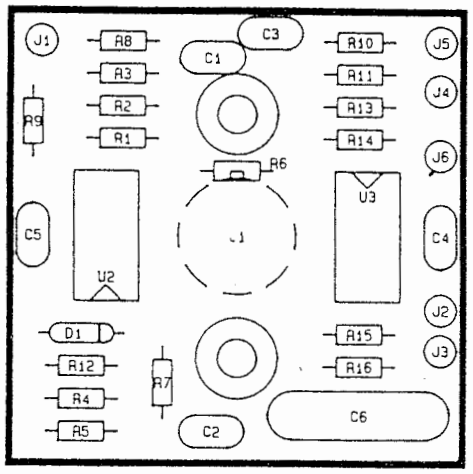

U1	EGG JUDSON, HUV-1100BQ (SOCKET), AUGAAT, 8059-269 MOUNTED ON OPPOSITE SIDE		
U2	BURR BROWN, OPA606 (SOCKET), SAMTEC, ICA-308-SGT		
U3	BURR BROWN, OPA606 (SOCKET), SAMTEC, ICA-308-SGT		
R1	15M OHMS, RC05	C1	.01uf, 1990
R2	15M OHMS, RC05	C2	.01uf, 1990
R3	15M OHMS, RC05	C3	.01uf, 1990
R4	12.5K OHMS, RC05	C4	.01uf, 1990
R5	12.5K OHMS, RC05	C5	220pf, 1990
R6	100 OHMS, RC05	C6	.005uf
R7	100 OHMS, RC05	D1	1N914
R8	70K OHMS, RC05		
R9	10K OHMS, RC05	J1	4531
R10	100 OHMS, RC05	J2	4531
R11	100 OHMS, RC05	J3	4531
R12	10K OHMS, RC05	J4	4531
R13	10K OHMS, RC05	J5	4531
R14	100K OHMS, RC05		
R15	100 OHMS, RC05		
R16			

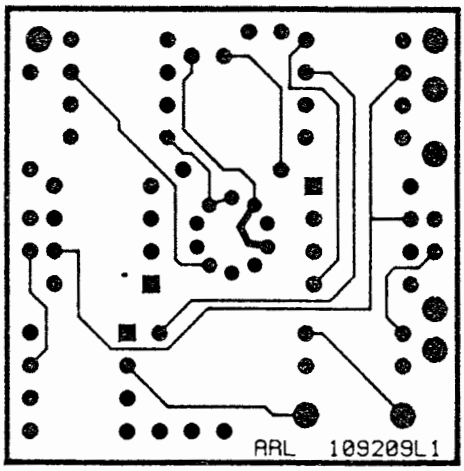

component side

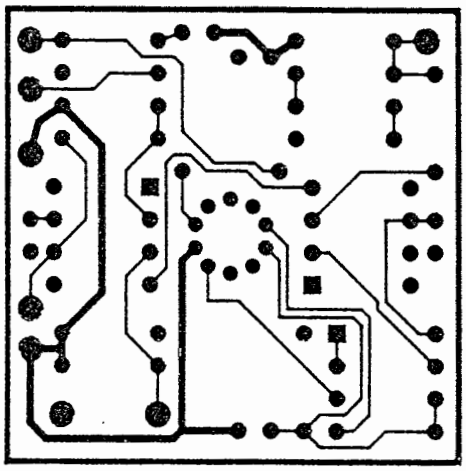

detector side

Figure B.1. Printed citcuit board design (1.7× scale). The board is a two-sided board. The largest component is the 0.047 μF polystyrene capacitor.

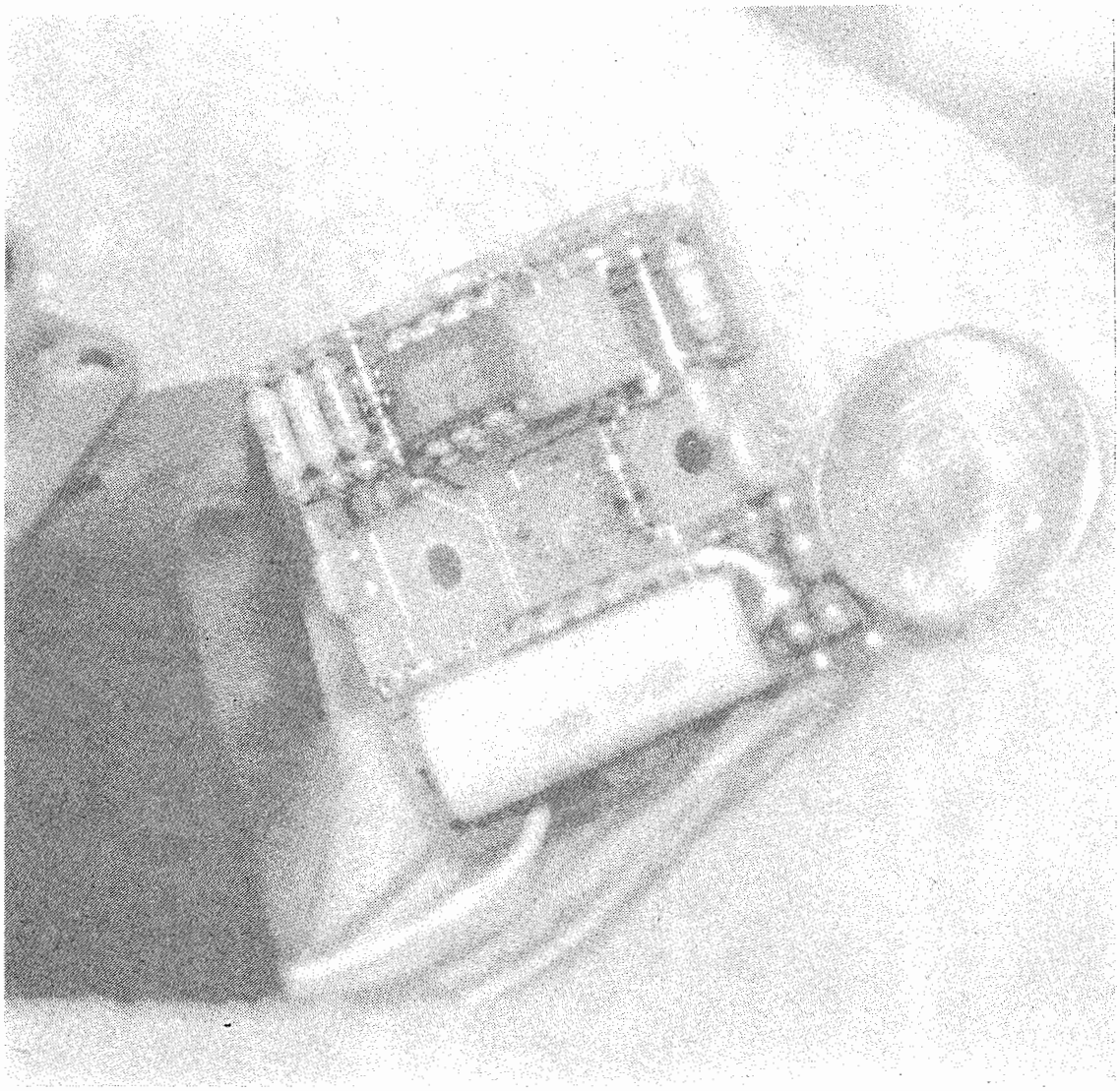

Figure B.2. Picture of completed circuit board. The largest component is the 0.047 μF polystyrene capacitor.

Appendix C
EXIT WINDOW DETECTOR

The peak detector circuit of Chapter 2 delivers a DC value corresponding to the peak of the pulses it detects anywhere in the optical path. After the circuit proved its proper operation in the energy monitor, it was easily applied to the an exit window detector. The simple purpose of the exit window detector is to indicate the presence of an obstruction or general uncleanliness on the window surface. Figure C.1 shows the assembly which includes a tubular mount that holds the 2" exit window, a 1/2" bored hole on the side of the mount resembling the filter assembly in Figure 2.5(b), and the detector box. The bored hole houses a 532 nm bandpass filter and neutral density filters, and it is angled such that the detector's detection cone encompasses the entire outside surface of the exit window that the laser beam passes through. The detector shows a very small signal from the laser scattering at the window surface when the window is clean. If something falls on the window to either block the beam or dirty the window, then the detector's signal rises with the increase in scattered energy. If the signal detects crosses a threshold set in the computer software, then the laser will stop. This prevents the laser from burning the object or "dirt" into the window coating and destroying an expensive optic. Figure C.2. is a picture of the actual detector box that screws into the exit window mount.

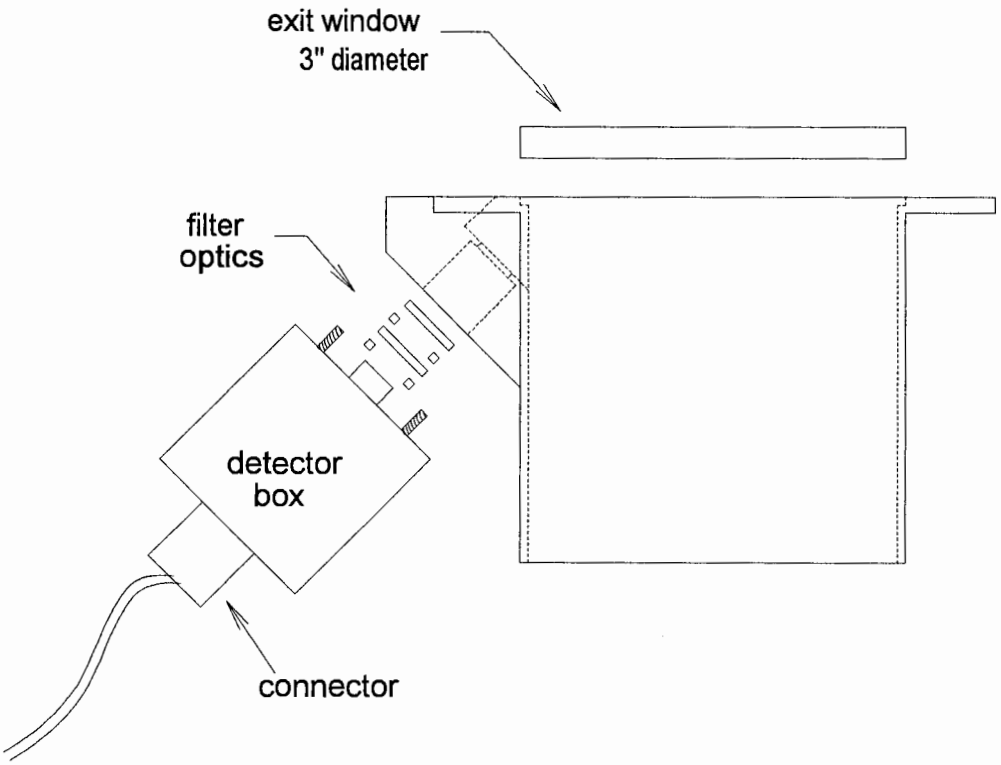

Figure C.1. Exit window assembly. After the laser beam passes through the beam expander, it is directed vertically through this assembly. Scattering at the top surface of the window is in the field-of-view of the detector.

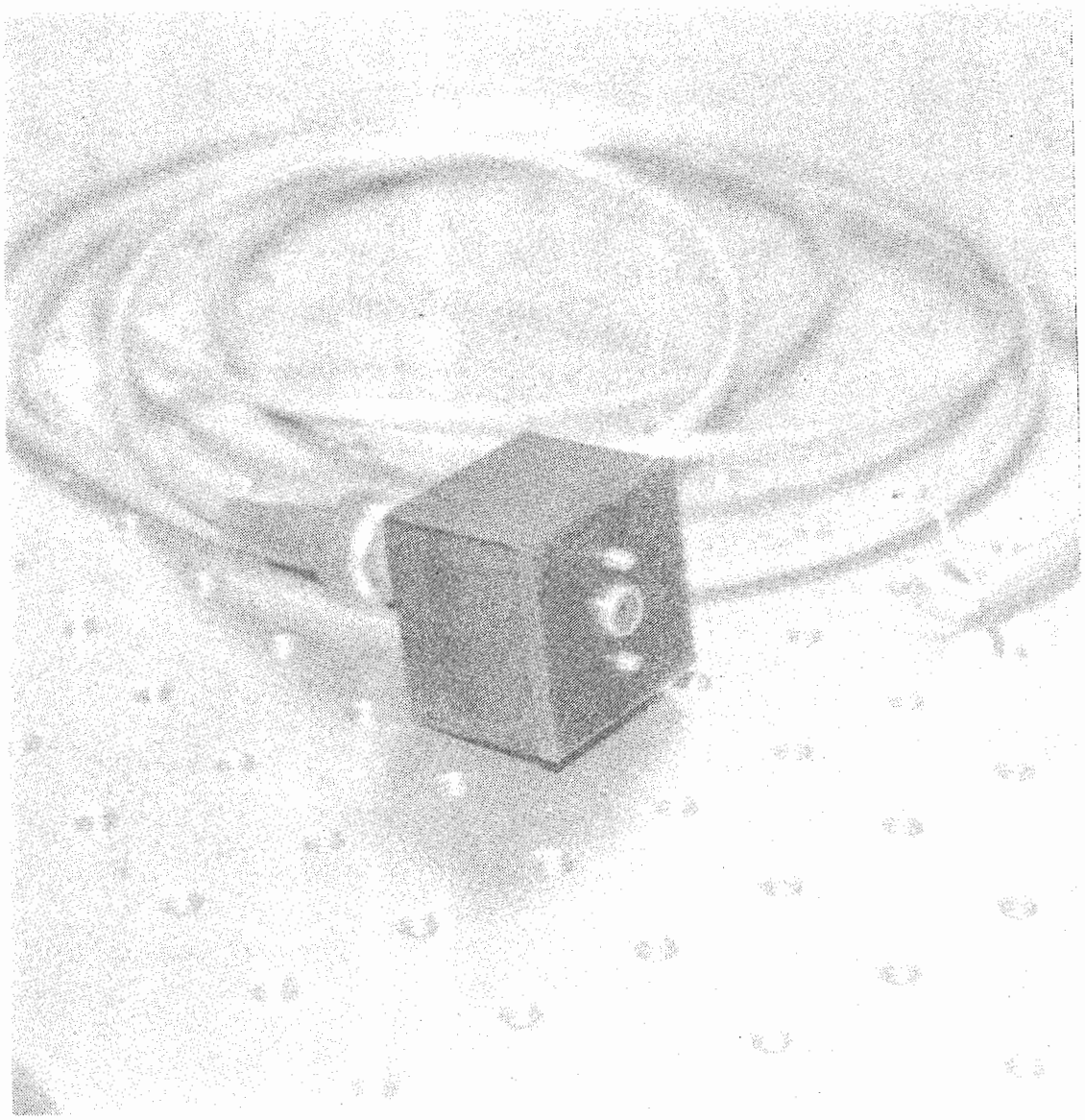

Figure C.2. The exit window detector box in this picture is virtually identical to the detector boxes on the energy monitor.

Appendix D

CONTROL PROGRAM LISTING

```
// 532 Control                                    Stephen Sprague 1/19/95
//
// Subroutine to find the peak conversion efficiency in the second harmonic generator.
//  (The following code is similar to C++ code, but not compilable).
//
// Preconditions: The subroutine receives a call from the main program that passes the
//    global variable OldPower (call by reference). The call may be at initial system setup
//    or during system operation. This subroutine assumes the temperature stability of the
//    crystal in the SHG.
// Postconditions: The subroutine returns a flag in indicate whether the SHG is peaked or
//    if no acceptable peak is found, synonomous with a time-out failure. Secondly, the
//    OldPower array is updated, the last value of which is the peak power achieved.

//declare these private variables - no initial values needed prior to calling 532Control
int step, sum, try, oldControl;
float fhgPower, power, dP, mean, threshold, maxPower;
char loop[5];

//declare these as private variables and initialize to zero
float oldPower[4];
bool endFlag;


bool 523Control(void)              // beginning of main function
{
try = 0;
peakFlag = 0;                      // flag set to "no peak" until peak found
oldControl = 1;
loop = " ";

while (loop != "Quit")
{
```

```
try = try + 1;
fhgPower = 266Power                    // calls data aquisition for power

if (fhgPower < 60)                     // these values in mJ
  maxPower = 435;                      //
else
  maxPower = 290;                      //

power = 532Power;                      // calls data aquisition for power

oldPower[3] = oldPower[2];             // update oldPower for history of power
oldPower[2] = oldPower[1];
oldPower[1] = oldPower[0];
oldPower[0] = power;

sum = 0;                               // Averages last 4 values for power
for (int i=0; i <4; i++)
  sum = sum + oldPower[i];
mean = sum/4;

threshold = 0.93 * maxPower;
if (mean > threshold)
{ peakFlag = 1;                        // SHG is peaked
  loop = "Quit";                       // exits subroutine
}

dP = power - oldPower[0];              // gradiant
step = round(maxPower/power);

if step < 1                            // Sets lower limit for step size
   step = 1;
elseif step > 1                        // Sets lower limit for step size
   step = 15;

if dP < 0
  control = -sign(oldControl)*step;    // Change direction, new step size
```

```
  else
    control = sign(oldControl)*step;          // Same direction, new step size
  Positioner(control,endFlag);          // Subroutine that moves SHG according to 'control'
                                        //     returns flag if hits end
  oldControl = control;                         // updates control history

  if (try > 40)                                 // timeout failure
    loop = "Quit";

  if (endFlag == 1)
  {  oldPower[0] = maxPower;                        // this will cause next try to go other
     endFlag  = 0;                                  //      direction
  }
}               // end while

return peakFlag;
}               // end subroutine
```